UNIVERSITÉ DE GENÈVE
INSTITUTE FOR ENVIRONMENTAL SCIENCES

The EUMETSAT Network of Satellite Application Facilities
CM SAF Climate Monitoring
4th user Workshop

Long term satellite hourly, daily and monthly global, beam and diffuse irradiance validation. Interannual variability analysis.

(Adapted to CM-SAF product from the IEA 2013 report)

Pierre Ineichen
University of Geneva
March 2014

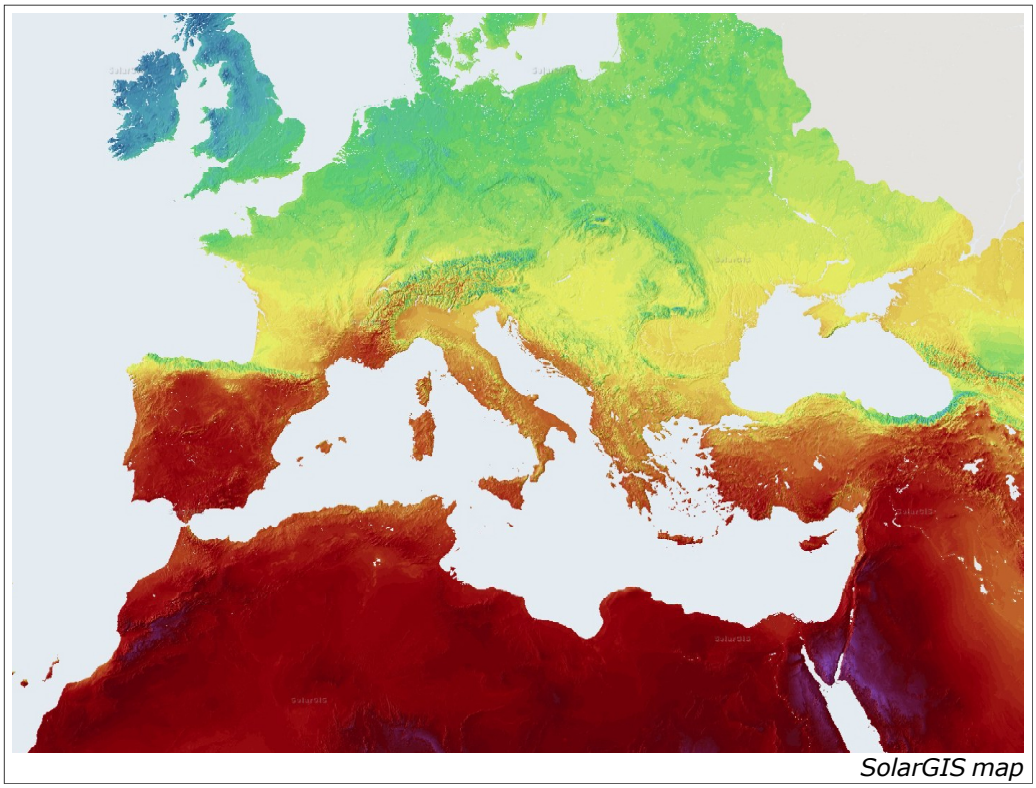

SolarGIS map

Long term satellite hourly, daily and monthly global, beam and diffuse irradiance validation. Interannual variability analysis.

(Adapted to CM-SAF product from the IEA 2013 report)

Pierre Ineichen
University of Geneva

Abstract

Satellite derived solar radiation is nowadays a good alternative to ground measurements for renewable energy applications. It has the advantage to provide data with a good accuracy, the best time and space granularity, in term of real time series and average year such as TMY.

This report presents results of a long term validation in the European and Mediteranean region of six nowcast satellite products in hourly, daily and monthly values, and six average products on an annual basis. The performance of all the products is put forward with the natural interannual variability; for comparison purpose, the SatelLight model is also included in the results.

The main results are:

- the accuracy of the derived global irradiance reaches 17% with no bias, and 34% for the beam component with a negligible bias,
- even with some high discrepancies for specific sites and models, on the average, all the products provide the annual global irradiation within one standard deviation of the interannual variability, with a bias standard deviation from 2% to 5%.
- eight of the nine models provide beam irradiance within one standard deviation, the best bias standard deviation is 6%.

Table of content

Nomenclature

G_h or *GHI*	global horizontal solar irradiance or irradiation
G_{hc}	clear sky global horizontal solar irradiance or irradiation
B_n or *DNI*	normal beam (or direct) solar irradiance or irradiation
D_h or *DIF*	diffuse horizontal solar irradiance or irradiation
B_{nc}	clear sky normal beam solar irradiance or irradiation
G_{sat}	modeled solar irradiance or irradiation
G_{mes}	measured solar irradiance or irradiation
I_o	extra-atmospheric solar irradiance
K	clearness or clear sky index
K_t	global clearness index (normalized by I_o)
$K_{t'}$	modified global clearness index
K_c	global clear sky index (G_h normalized by G_{hc})
K_d	diffuse clearness index
K_b	beam clearness index
K_{bc}	beam clear sky index (B_n normalized by B_{nc})
T_L	Linke turbidity coefficient
T_{Lam2}	Linke turbidity coefficient at air mass = 2
aod	atmospheric aerosol optical depth
w	atmospheric water vapor content or column
δ_{cda}	aerosol optical depth of a clean and dry atmosphere
δ_w	water vapor atmospheric optical depth
T_a	ambiant temperature at 2m
RH	relative humidity at 2m
h	solar elevation angle
AM	atmospheric air mass
n	cloud index or cloud albedo (same as *CAL*)
CAL	cloud albedo or cloud index (same as *n*)
ρ	planetary albedo
ρ_g	overcast sky planetary albedo
ρ_c	clear sky planetary albedo
mbd	mean bias difference
rmsd	root mean square difference
sd	standard deviation
bsd	bias standard deviation (standard deviation of the bias)
R	correlation coefficient

1. Introduction

Meteorological satellite images as data sources to evaluate the ground irradiance components become the state of the art in the field of solar energy systems. The strongest argument is the high spatial coverage, and the fifteen minutes temporal granularity. They also have the advantage to provide nowcast data used for example to assess the proper operation of a solar plant. On the other hand, long term ground data are very scarce concerning the beam irradiance. The use of secondary inputs such as polar satellite data and ground information increases significantly the precision of the algorithms, mainly for the beam component. Following a paper from Zelenka (1998) concerning the nuggets effect, the interpolation distance to the nearest ground measurement site is limited to 10 to 30 km, depending on the irradiance parameter; this strengths the satellite derived data argument.

Many Universities and private companies provide satellite derived data, freely or for pay, averaged over 8 years (Meteosat second generation is operational since April 2004) or in real time (nowcasting), and integrated over different time ranges. We choose six European data providers to conduct a long term validation (2004 - 2011) against ground measurements, for both the global and the beam components, and based on hourly, daily and monthly values.

2. Ground data

Data acquired at eighteen ground sites are used for the validation, with up to 16 years of continuous measurements; for the validation itself, due to the satellite variability, only data from 2004 to 2011 are used. The data acquired before 2004 are

Site	Gh	Bn	Dh	latitude	longitude	altitude	climate	origin
Almeria (Spain)	x	x	x	37.092	-2.364	491	dry, hot summer	PSA
Bratislava (Slovakia)	x		x	48.166	17.083	195	semi-continental	CIE
Carpentras (France)	x	x	x	44.083	5.059	100	mediternean	BSRN
Davos (Switzerland)	x	x	x	46.813	9.844	1586	alpine	PMO/SLF
Geneva (Switzerland)	x	x		46.199	6.131	420	semi-continental	CIE
Kassel (Germany)	x	x	x	51.312	9.478	173	temperate humide	FhG
Lerwick (Great Britain)	x	x	x	60.133	-1.183	82	cold oceanic	GAW
Lindenberg (Germany)	x	x	x	52.210	14.122	125	moderate maritim	BSRN
Madrid (Spain)	x	x	x	40.450	-3.730	650	semi-arid	UMP
Nantes (France)	x		x	47.254	-1.553	30	oceanic	CSTB
Payerne (Switzerland)	x	x	x	46.815	6.944	490	semi-continental	BSRN
Sede Boqer (Israel)	x	x	x	30.905	34.782	457	dry steppe	BSRN
Tamanrasset (Algeria)	x	x	x	22.780	5.510	1400	hot, desert	BSRN
Toravere (Estonia)	x	x	x	58.254	26.462	70	cold humid	BSRN
Valentia (Ireland)	x		x	51.938	-10.248	14	oceanic	GAW
Vaulx-en-Velin (France)	x	x	x	45.778	4.923	170	semi-continental	ENTPE
Wien (Austria)	x		x	48.250	16.367	203	continental	GAW
Zilani (Letonia)	x	x	x	56.310	25.550	107	cold humid	GAW

Table I List of the ground sites with the latitude, longitude, altitude, climate, the acquired parameters and the origin of the data

used to illustrate the interannual variability. The list of the stations is given in Table I, with their characteristics. The climate range covers desert to oceanic, the latitude from 20°N to 60°N, and the altitudes from sea level to 1580 meters.

The concerned parameters are the global irradiance on a horizontal plane G_h (or GHI), the normal beam irradiance B_n (or DNI) and the horizontal diffuse irradiance D_h (or DIF). For some sites, only the beam or the diffuse component is acquired.

The ground data are kindly provided by the Baseline Surface Radiation Network (BSRN), the Global Aerosol Watch project (GAW), the CIE International Daylight Measurements Program (Commission internationale de l'éclairage IDMP), the Centre Scientifique et Technique du Bâtiment (CSTB) in Nantes, the Universidad Politécnica de Madrid (UMP), the Ecole National des Travaux Publiques (ENTPE) of Lyon, the Deutsches Zentrum für Luft und Raumfahrt (DLR), the Frauhenhofer Institute in Freiburg, the Institute of Construction and Architecture of the Slovak Academy of Sciences, the Institut für Schnee- und Lawinenforschung (SLF) and the Physikalisch-Meteorologisches Observatorium Davos (PMOD).

High precision instruments (WMO standards) such as Kipp+Zonen CM10, Eppley PSP pyranometers, and Eppley NIP pyrheliometers, are used to acquire the data. A stringent calibration, characterization and quality control was applied on all the data by the person in charge of the measurements; the coherence of the data for all the stations was verified by the author and is described in section 5.

3. Satellite data: nowcasting or «real time» models

For the «real time» comparison, six different products are validated in the present study. The methodology and the input parameters are described in the following section. DLR provide data derived with three different climatologies for Solemi, University of Oldenburg provided data EnMetSol based on two different clear sky models. Only the best results are kept in this report.

3.1 SolarGis

In SolarGis (GeModel Solar), the irradiance components are the results of a five steps process: a multi-spectral analysis classifies the pixels, the lower boundary (*LB*) evaluation is done for each time slot, a spatial variability is introduced for the upper boundary (*UB*) and the cloud index definition, the Solis clear sky model is used as normalization, and a terrain disaggregation is finally applied.

Four MSG spectral channels are used in a classification scheme to distinguish clouds from snow and no-snow cloud-free situations. Prior to the classification, calibrated pixel values were transformed to three indices: normalized difference snow index (Ruyter 2007), cloud index (Derrien 2005), and temporal variability index. Exploiting

the potential of MSG spectral data for snow classification removed the need of additional ancillary snow data and allowed using spectral cloud index information in cases of complex conditions such as clouds over high albedo snow areas.

In the original approach by Perez (2002), the identification of surface pseudo-albedo is based on the use of a lower bound (*LB*), representing cloudless situations. This approach neglects diurnal variability of *LB* that is later corrected by statistical approach. Instead of identifying one value per day, *LB* is represented by smooth 2- dimensional surface (in day and time slot dimensions) that reflects diurnal and seasonal changes in *LB* and reduces probability of no cloudless situation.

Overcast conditions represented in the original Perez model by a fixed Upper Bound (*UB*) value were updated to account for spatial variability which is important especially in the higher latitudes. Calculation of cloud index was extended by incorporation of snow classification results.

The broadband simplified version of Solis model (Ineichen 2008a) was implemented. As input of this model, the water vapor is derived from CFSR and GFS databases from NOAA NCEP, and the atmospheric optical depth is calculated from MACC database from ECMWF (Cebecauer 2011)

Simplified Solis model was also implemented into the global to beam Dirindex algorithms to calculate Direct Normal Irradiance component (Perez 1992, Ineichen 2008c). Diffuse irradiance for inclined surfaces is calculated by updated Perez model (1987).

Processing chain of the model includes post-processing terrain disaggregation algorithm based on the approach by Ruiz-Arias (2010). The disaggregation is limited to shadowing effect only, as it represents most significant local effect of terrain. The algorithm uses local terrain horizon information with spatial resolution of 100 m. Direct and circumsolar diffuse components of global irradiance were corrected for terrain shadowing. Snow cover is taken from GFS and CSFR (NOAA).

3.2 Helioclim-3

The Helioclim 3 data bank is produced with the Heliosat-2 method that converts observations made by geostationary meteorological satellites into estimates of the global irradiation at ground level. This version integrates the knowledge gained by various exploitations of the original Heliosat method and its varieties in a coherent and thorough way.

It is based upon the same physical principles but the inputs to the method are calibrated radiances, instead of the digital counts output from the sensor. This change opens the possibilities of using known models of the physical processes in atmospheric

optics, thus removing the need for empirically defined parameters and of pyranometric measurements to tune them. The ESRA models (ESRA 2000, Rigollier 2000 and 2004) are used for modeling the clear-sky irradiation. The assessment of the ground albedo and the cloud albedo is based upon explicit formulations of the path radiance and the transmittance of the atmosphere. The turbidity is based on climatic monthly Linke Turbidity coefficients data banks.

The Liu and Jordan (1960) model is used to split the global irradiance into the diffuse and beam components.

3.3 Solemi

The transfer of the extraterrestrial solar irradiance to the Earth's surface is influenced by various constituents of the atmosphere. Ozone, aerosol and water vapor are modelled with long time climatological and reanalysis data sets. Clouds which have the largest influence and highest variability are determined from the half hourly Meteosat images. Both visible and infrared channels are used to improve the detection at sunrise and sunset and of high cirrus clouds.

For the global irradiance G_h, an algorithm based on the Heliosat method (Cano et al. (1986, Hammer et al. 2000 and 2003) is implemented. Contrary to the majority of the other schemes, the beam component is directly derived from the satellite images by the method of Schillings et al. (2003). Instead of using a general turbidity index like most other procedures, each important constituent is treated separately with the help of the Bird clear sky model (1984).

The atmospheric water vapor *w* is taken from the NOAA-NCEP (National Oceanic and Atmospheric Administration - National Centers for Environmental Prediction) NCDC data (National Climatic Data Center), and the impact of aerosols (*aod*) is taken from NASA-GISS (National Aeronautics and Space Administration – Goddard Institute for Space Studies) GACP-data (Global Aerosol Climatological Project). From these data sets the transmission of the cloud-free atmosphere is calculated.

The cloud parameterization scheme is a two-channel procedure, which uses the visible channel of Meteosat (0.45 µm to 1 µm) and the infrared channel (10.5 µm to 12.5 µm.).

3.4 IrSOLaV

In the IrSolAv irradiance derivation scheme, the cloud index *n* is derived using the methodology developed by Dagestad and Olseth (Dagestad and Olseth, 2007) with some modifications in the ground albedo determination. The ground albedo is computed from a forward and backward moving window of 14 days taking into account its evolution during the day, as function of the co-scattering angle.

The global horizontal irradiance G_h is then evaluated from the cloud index with the model proposed by Zarzalejo (Zarzalejo et al., 2009); it uses as independent variables the cloud index, the 50-percentile of the cloud index for a given place, and the air mass *AM*. The normal beam irradiance B_n is calculated from the global irradiance with the help of Louche correlation (Louche et al., 1991).

In a second step, the clear sky conditions are identified with the algorithm proposed by Polo (Polo et al., 2009a; Polo et al., 2009b); for these clear conditions, the irradiances are evaluated with the ESRA clear sky model (Rigollier 2000), using the aerosol optical depth *aod* taken from Soda, MODIS or from a method proposed by Polo (Polo et al., 2009a) depending on their availability.

3.5 EnMetSol

The EnMetSol method is a technique for determining the global radiation at ground by the use of data from a geostationary satellite (Beyer 1996, Hammer 2003). It is used in combination with a clear sky model to evaluate the 3 irradiance parameters G_h, D_h and B_n. The key parameter of the method is the cloud index *n*, which is estimated from the satellite measurements and related to the transmissivity of the atmosphere via

$$K_c = 1 - n$$

where the transmissivity is expressed by the clear sky index K_c defined as the ratio of global irradiance G_h and the corresponding clear sky irradiance G_{hc}:

$$K_c = \frac{G_h}{G_{hc}}$$

Two sets of data produced with the EnMetSol algorithm will be analyzed, corresponding to two different clear sky irradiance models:

- the model of Dumortier (Fontoynont 1998, Dumortier 1998) with the Remund (2009) Meteonorm HR high resolution data base for the turbidity input,
- and the original Solis clear sky model (Mueller 2004) with monthly averages of *aod* (Kinne 2005) and water vapour content (Kalnay 1996) as input parameters.

For the Dumortier clearsky, a diffuse fraction model (Lorenz 2007) is used to calculate the all sky diffuse horizontal irradiance (via G_h - D_h). A recently developed beam fraction model (Hammer 2009) is used to calculate the B_n for all sky conditions with the Solis model.

3.6 Heliomont

In the Heliomont MeteoSwiss process (Stoeckli 2013), the all sky incident surface solar radiation fluxes at the earth's surface are calculated by combining the clear sky surface radiation fluxes from a radiative transfer model with the radiative cloud forcing derived from satellite data. This method is commonly referred to as "Heliosat" (Cano

et al., 1986), and was successively adapted for the EUMETSAT MFG satellite (Möser and Raschke, 1984). It relies on the so-called "cloud index" which exploits the radiative properties of clouds in the visible solar spectrum. When viewed from space, the cloud transmittance is inversely related to the cloud reflectance. It empirically accounts for the absorption, reflection and scattering of solar radiation in clouds under the assumption that clouds are substantially brighter than the underlying surface.

For bright surfaces, the infrared cloud index replaces the visible (classical) cloud index. Often a slot-wise approach is used to composite the clear sky reflectance for each time step from e.g. the last month's reflectance values. In "HelioMont" the clear sky compositing calculates a diurnal course of the clear sky reflectance and the clear sky brightness temperature from cloud masked reflectance and brightness temperature values of the previous days. This guarantees that the clear sky reflectance and brightness temperature values have consistency on the diurnal time scale. This also enables to account for short-term changes in surface reflectance, such as during green-up or during periods of snow fall. In "HelioMont" the maximum cloud reflectance depends on solar- and view-geometry. Maximum cloud reflectance fields are calculated with a radiative transfer model simulating the radiative properties of ice and water clouds with an optical thickness of 128 at each time step (Mayer and Kylling, 2005). In "HelioMont" the maximum cloud reflectance is thus spatially distributed and relies on inter-calibrated radiances.

A single atmospheric turbidity parameter like the Linke turbidity cannot account for the molecular absorption and scattering effects of the individual atmospheric constituents on global radiation and its components (Müller et al., 2004). Also, the climatological state of the atmosphere can strongly deviate from its instantaneous state with adverse effects on the quality of the calculated clear sky solar radiation fluxes. We thus make use of a radiative transfer model (Mayer and Kylling, 2005), parameterized by the so-called Modified Lambert-Beer (MLB) set of equations in combination with a look-up table (LUT) for efficient processing (Müller et al., 2009). Specifically, a modified version of the publicly available gnu-MAGIC algorithm (http://sourceforge.net/projects/gnu-magic/) with a re-calculated LUT is used. It is constrained by 6-hourly total column water vapor and ozone data from the European Centre for Medium-range Weather Forecast (ECMWF) and by use of monthly aerosol climatology (Kinne, 2008).

3.7 CM-SAF

The CM-SAF algorithm is based on the Heliosat method (Cano et al.,1986) which has been enhanced in several domains (Beyer et al., 1996, Hammer et al., 1998 and 1999). The method is basically driven by the strong complementarity between the planetary albedo recorded by the satellite's radiometer and the surface shortwave radiant flux. The planetary albedo ρ increases with increasing atmospheric turbidity and cloud cover. Therefore an effective cloud albedo *CAL* (or cloud index *n)* is introduced

as a measure of the cloud cover derived from Meteosat visible counts:

$$CAL = \frac{\rho - \rho_g}{\rho_c - \rho_g}$$

where ρ_g and ρ_c are respectively the relative reflectivity in the clear sky and overcast case. The CM-SAF climate version of the method includes several improvements: a self-calibration of ρ_c, the highest possible cloud reflectivity. In the Rigolier's method (see section 3.2), the upper limit is used as ρ_c, here only the 95%-percentile in a specific cloudy target region and is set to ρ_c.

For the retrieval of the ground albedo ρ_g (or clear sky reflectivity), in order to take into account the changes of the vegetation, instead of a monthly window used ine the heliosat method, a seven day moving average is used in the algorithm. This enables also to take into account the ground snow cover.

The clear sky irradiance G_{hc} is calculated using an eigenvector lookup table (*LUT*) method (Mueller et al., 2009). It is based on the libRadtran radiative transfer model (Mayer & Kylling, 2005) and enables the use of extended information about the atmospheric state.

3.8 Satellight

In the same way, the Satellight algorithms for retrieving global irradiance from satellite is based on the Heliosat method to retrieve a cloud index *n*.The clear sky index *K* is then defined as the ratio of surface global horizontal irradiance to the corresponding clear sky irradiance as derived by Page (1996) and Dumortier (1995) for respectively the beam and the diffuse components. The global irradiance is then derived from the cloud index *n* (or *CAL*) following Fontoynont (1998).

In the cloudless case the diffuse irradiance can be derived from Dumortier (1995). Skartveit and Olseth (1987) suggested an all sky model for the diffuse fraction of hourly global radiation, assuming that the diffuse fraction depends on the clearness index and the solar elevation. For a clearness index K_t below a certain threshold the hourly radiation is expected to be completely diffuse. With increasing clearness index the diffuse fraction decreases. For high clearness index values it increases again due to cloud reflection effects. The position of the minimum of diffuse fraction depends on the solar elevation. An improved version of this model also accounts for the hour-to-hour variability of the clearness index (Skartveit et al., 1998).

4. Satellite data: average and typical years

Depending on the application, average and typical years are used as input to simulations. These are generally obtained from 10 to 20 years of measurements, averaged and partially interpolated between stations. Some of them are corrected with the help of meteorological and polar satellite data and/or ground information.

The data included in the comparison are derived within networks, programs or software described below.

4.1 PVGIS

Photovoltaic Geographical Information System provides a map-based inventory of solar energy resource and assessment of the electricity generation from photovoltaic systems in Europe, Africa, and South-West Asia (available from http://re.jrc.ec.europa.eu/pvgis/index.htm). For Europe, a new data set is available in version 4, evaluated by Eumetsat climate satellite facilities (CMSAF, DWD).

4.2 WRDC

The World Radiation Data Centre Online Archive contains international solar radiation data stored at the WRDC, which is a central depository for data collected at over one thousand measurement sites throughout the world (available from http://wrdc-mgo.nrel.gov/).

4.3 RetScreen

The RETScreen Clean Energy Project Analysis Software is a unique decision support tool developed with the contribution of numerous experts from government, industry, and academia. The software, provided free-of-charge, can be used worldwide to evaluate the energy production and savings, costs, emission reductions, financial viability and risk for various types of Renewable-energy and Energy-efficient Technologies (RETs, available from http://www.retscreen.net).

4.4 NASA SSE

is a renewable energy resource web site of global meteorology and surface solar energy climatology from NASA satellite data on 1 by 1 degree resolution (available from http://eosweb.larc.nasa.gov/sse/).

4.5 Meteonorm

Meteonorm (v7) is a comprehensive meteorological reference software, incorporating a catalogue of meteorological data and calculation procedures for solar applications and system design at any desired location in the world. It is based on over 23 years of experience in the development of meteorological databases for energy applications (see http://www.meteonorm.com).

4.6 ESRA

The European Solar Radiation Atlas is oriented towards the needs of the users like

solar architects and engineers, respecting the state of the art of their working field and their need of precise input data. From best available measured solar data complemented with other meteorological data necessary for solar engineering, digital maps for the European continents are produced. Satellite-derived maps help in improving accuracy in spatial interpolation (see http://www.helioclim.com).

4.7 Averaged nowcast models

For the six nowcasting modelled data sets described section 3, the data are either aggregated into monthly values, or directly retrieved from the provider in monthly values.

5. Data quality control

Sensor calibration is the key point for precise data acquisition in the field of solar radiation. The radiation sensors should be calibrated by comparison against a sub-standard before the beginning of the acquisition period, and then every year. Due to possible errors and inaccuracies, a post-calibration is difficult to conduct.

The validity of the results obtained from the use of measured data is highly correlated with the quality of the data bank used as reference. Controlling data quality is therefore the first step to perform in the process of validating models against ground data. This essential step should be devised properly and automated in order to rapidly detect significant instrumental problems like sensor failure or errors in calibration, orientation, leveling, tracking, consistency, etc. Normally, this quality control process should be done by the institution responsible for the measurements. Unfortunately, it is not the case at many stations. Even if some quality control procedures have been implemented, it might not be sufficient to catch all errors, or the data points might not be flagged to indicate the source of the problem. A stringent control quality procedure must therefore be adopted in the present context, and its various elements are described in what follows.

If the three solar irradiance components—beam, diffuse and global—are available, a consistency test can be applied, based on the closure equation that link them:

$$B_n = \frac{G_h - D_h}{\sin(h)}$$

where B_n, G_h and D_h are respectively the normal beam irradiance, the horizontal global and diffuse irradiance, and h the solar elevation angle over the horizon.

An a posteriori automatic quality control cannot detect all acquisition problems that could have happened, however. The remaining elements to be assessed are threefold:

- the measurement's time stamp (needed to compute the solar geometry),

- the sensors' calibration coefficient used to convert the acquired data into physical values,
- the coherence between the parameters.

5.1 Time stamp

To detect a possible time shift in the data, the symmetry (with respect to solar noon) of the irradiance for very clear days is visually checked. The global horizontal and direct normal irradiances are plotted versus the sine of the solar elevation angle for specific clear days. If the time stamp is correct, the afternoon curve should normally lay over the morning curve as visualized in Figure 1. Exceptions do occur, however, at sites where the atmospheric turbidity changes during the day, due for example to topography-induced effects, where the clear-sky irradiance can be significantly different in the afternoon than in the morning. As the global irradiance is less sensitive to turbidity, the accordance morning/afternoon is of more importance for the global component.

If this test is positive, verification can be done with the help of the global clearness indices K_t and K_b defined respectively as:

$$K_t = \frac{G_h}{I_o \cdot \sin(h)} \qquad K_b = \frac{B_n}{I_o}$$

where I_o is the extraterrestrial solar irradiance (i.e., the solar constant corrected for the actual sun-earth distance). The clearness index is then plotted for the morning

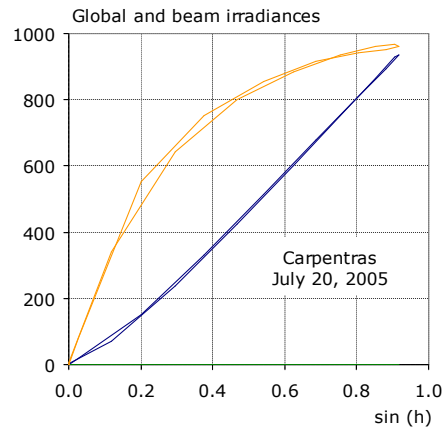

Figure 1 above: G_h and B_n represented versus the sinus of the solar elevation angle for a clear day.

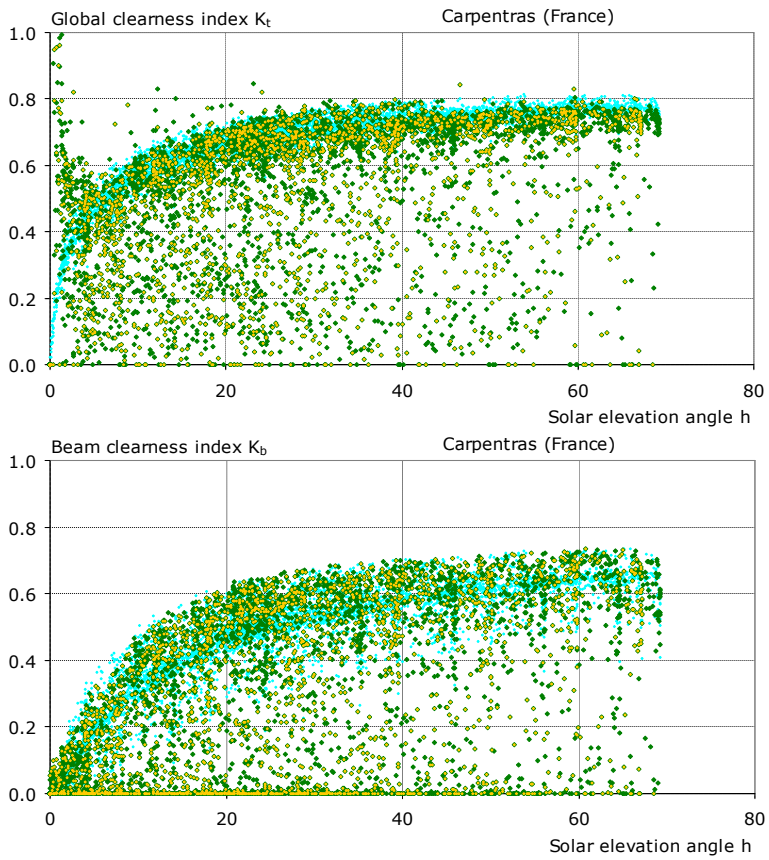

Figure 2 right: K_t and K_b represented separately for the morning (green) and the afternoon (yellow) data, versus the solar elevation angle for one year of hourly values in Carpentras. Corresponding clear sky model data are represented in light blue.

and afternoon data separately, e.g. using different colors. The upper limit, representative of clear-sky conditions, should lay over for the morning and the afternoon data as represented in Figure 2 for one year of global irradiance data acquired at Carpentras (France). Ideal hourly clear-sky values, calculated with the Solis model, are plotted in blue on the same graph. This test is very sensitive since a time shift of only a few minutes will conduct to a visible asymmetry.

When these two conditions (symmetry around solar noon and consistency of envelope) are fulfilled, the time stamp of the data bank can be considered correct, and the solar geometry can be precisely calculated.

5.2 Sensor calibration

The sensors' calibration can be verified for clear sky conditions by comparison against data from a nearby station or with the help of additional measurements. To conduct this test, for each day, the highest hourly value of G_h and B_n is selected from the measurements and plotted against the day of the year as illustrated in Figure 3. These points are representative of the clearest daily conditions. As the highest value for each day is selected, the upper limit normally represents clear-sky conditions (for G_h, it happens that higher-than-clear-sky values are obtained under partly cloudy or scattered clouds, high-sun conditions, this is why this test should not be applied for data with time granularity lower than hourly). On such graphs, data from nearby sites, or from different years for the same site can be compared.

The G_h graphs can be augmented by superimposing the modified clearness index K_t', which was defined by Perez and Ineichen (1990) as:

$$K_t' = \frac{K_t}{(1.031 \cdot \exp(-1.4 / (0.9 + 9.4 / AM)) + 0.1)}$$

where *AM* is the optical air mass as defined by Kasten (1980). This modified clearness index has the advantage of being relatively more independent from the solar elevation

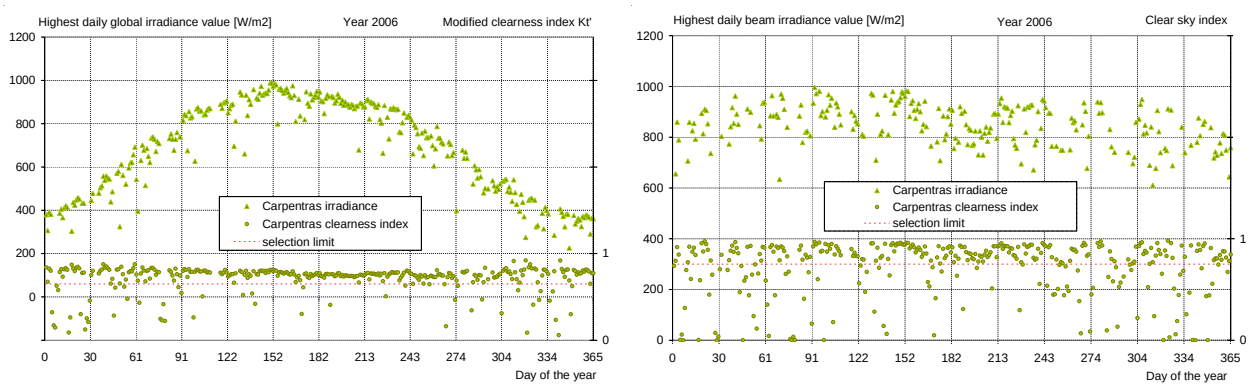

Figure 3 Daily highest value of respectively the global and the beam irradiances reported versus the day of the year for the station of Carpentras. The corresponding modified clearness index and clear sky index are also represented.

angle than K_t. Therefore, it is possible to delineate three K_t' zones to characterize the sky condition (Ineichen 2009):

clear-sky conditions	$0.65 < K_t' \leq 1.00$
intermediate sky conditions	$0.30 < K_t' \leq 0.65$
cloudy sky conditions	$0.00 < K_t' \leq 0.30$

In the upper part of Figure 3, only values with $K_t' > 0.65$ are represented.

For B_n, the clear-sky index is defined as:

$$K_{bc} = \frac{B_n}{I_o \; e^{\,-\,MA \cdot (\delta_{cda} + \delta_w)}}$$

where δ_{cda} is the broadband clean and dry atmosphere optical depth, and δ_w is the water vapor optical depth. These two broadband optical depths can be evaluated following Molineaux (1998) with simplified expressions:

$$\delta_{cda} = -0.101 + 0.235 \cdot AM^{\,-0.16} \qquad \delta_w = 0.112 \cdot AM^{\,-0.55} \cdot w^{\,0.34}$$

The denominator of K_{bc} is representative of the beam irradiance transmitted by a clean atmosphere. K_{bc} is represented on the right graph of Figure 3. On the upper part, only values for K_{bc} higher than 0.8 are represented.

The sensor calibration's correctness can then be assessed by comparison if data from a nearby site are available. If not, this can alternatively be done with the help of a clear-sky radiative model when the atmospheric aerosol optical depth (*aod*) and the water vapor column (*w*) are known. The long term stability of the calibration can also be assessed with this method by plotting on the same graph several years of data.

In the first case, it can be assumed that clear conditions result in similar irradiances if the sites are not too far one from the other, and are in similar climate situations. The upper limits of the compared plots should therefore coincide. This is illustrated on Figure 4 for the sites of Toravere and Zilani, situated at 200 km one from the other and under similar climates.

In the second case, *aod* and *w* data may be retrieved from independent ground-based sunphotometer networks such as Aeronet, if a station is close to that of the radiometric station being investigated. These quantities are measured automatically at 15-minute intervals by Aeronet stations. Since only data acquired under direct sun conditions are valid, the original data stream (Level-1) is analyzed to filter out non-sun conditions (Level-1.5). Further corrections are applied to reflect any change in calibration or quality-control issues (Level-2). Level-2 data should be used whenever possible since they are of the best possible quality. Individual values are then averaged to obtain a daily value. The same can be done for *w*. In case it is not measured by a

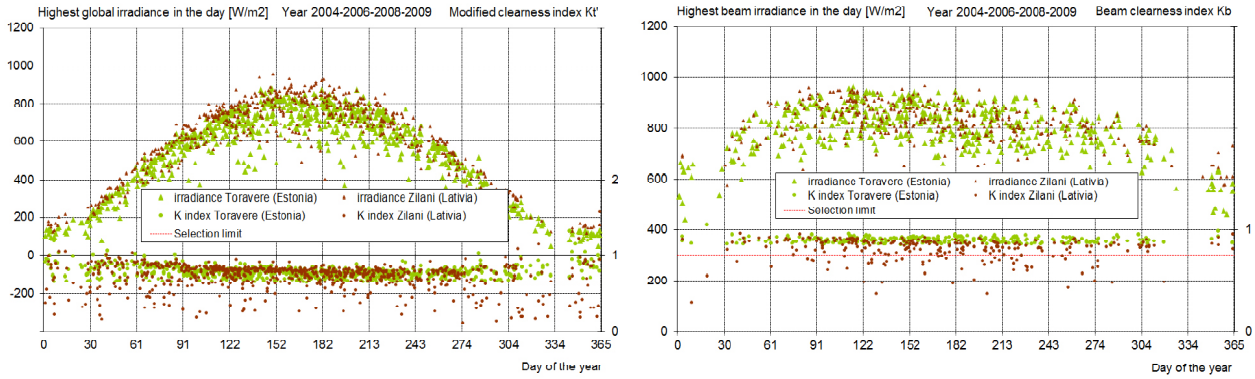

Figure 4 Comparison of measurements from two nearby (200km) stations: daily highest value of the global irradiance reported versus the day of the year for the station of Toravere and Zilani, for the irradiance components and the corresponding modified clearness index.

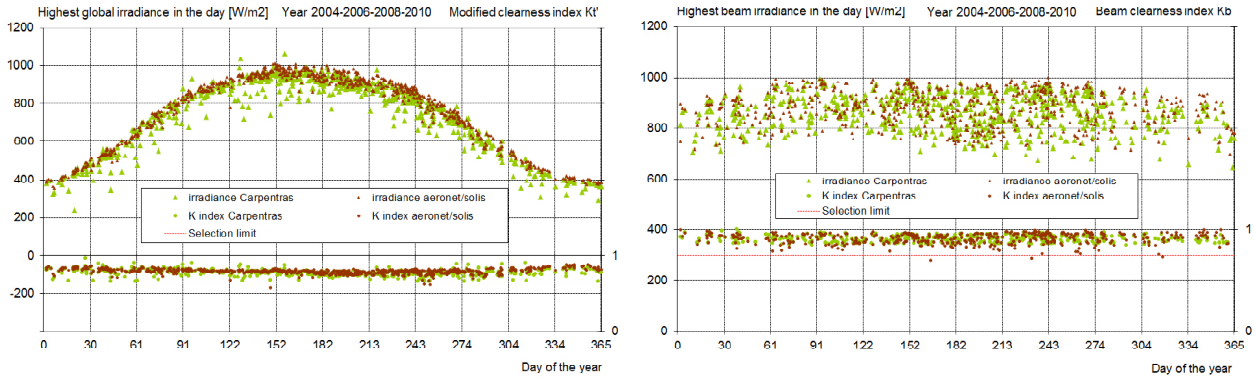

Figure 5 Comparison of the clear sky irradiance obtained from BSRN measurements and evaluated with the solis model with aeronet data

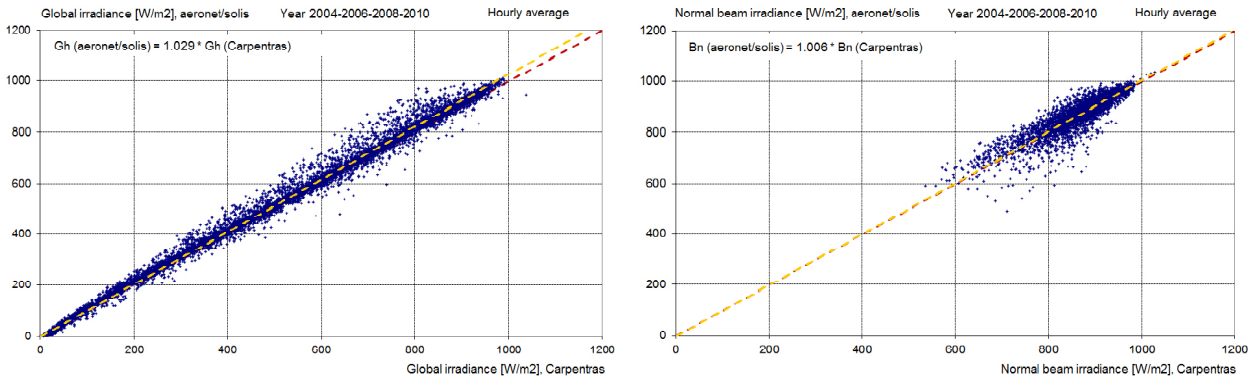

Figure 6 Scatter plots of the two data sets for the global and the beam components. The slope given on the graph is representative of the calibration coefficient difference.

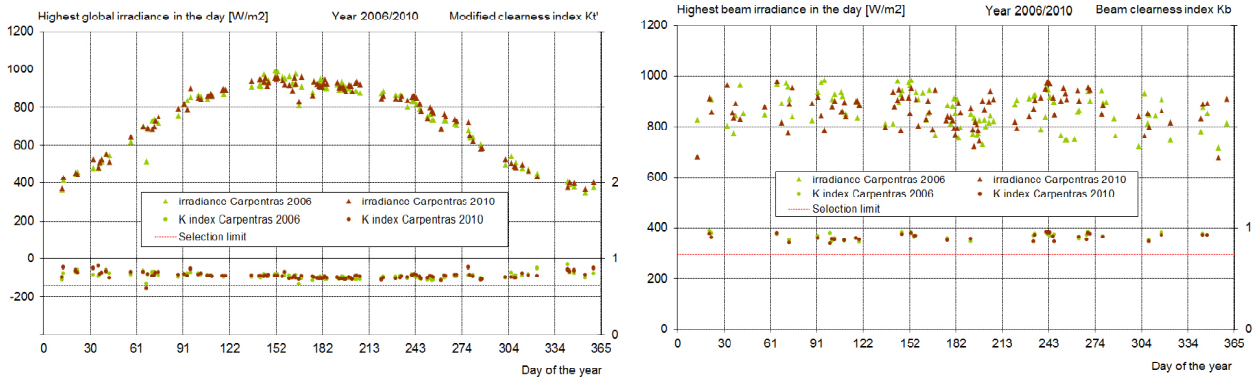

Figure 7 Comparison between two differents years of BSRN measurements: same representations as above

nearby Aeronet or similar network, it can be evaluated from the ground ambient temperature T_a and relative humidity *RH* by the use of an empirical model, such as Atwater's model (Atwater 1976). The latter method is approximate, but spatially extrapolating actual measurements also introduces errors, so that there is no perfect method in most cases. When temperature and/or humidity data are missing, the data from a neighboring station can be used, or as a last resort (and much larger errors), monthly average from climatic data banks. These *aod* and *w* values are then used with a clear sky model (Solis clear-sky radiative model (Muller 2004, Ineichen 2008), or CPCR2 (Gueymard 1989) to evaluate the clear-sky hourly G_h and B_n values. These are plotted on the same graphs than above, as shown in Figure 5 for measurements from Carpentras. On these graphs, the upper limits of the irradiance values and of the clearness indices obtained with the two methods should be similar.

To quantitatively assess the correctness of the calibration factor, a linear regression is applied on the clear condition selected hourly values, between the two sets to be compared. This is illustrated in Figure 6 for the two components. The slope of the regression line is also shown for each case.

In the latter case, the irradiance components can be compared year by year for the same site in order to assess the stability of the measurements. Here again, the upper boundary should not change from one year to the other, if there are no significant changes in the turbidity and/or the humidity. An example is given on Figure 7 for measurements acquired in 2006 and 2010 at Carpentras. Considering the whole period used in the validation, a calibration coefficient shift can be pointed out by this method.

5.3 Components consistency

The consistency test between the G_h and B_n components can be verified with the help of the global and beam clearness indices.

The hourly beam clearness index is plotted versus the corresponding global index as illustrated for the site of Carpentras in Figure 8. On the same graph, the clear-sky predictions from the Solis radiative model are represented for four different a priori values of *aod*. The corresponding Linke turbidity coefficient T_{Lam2} is then calculated from the B_n thus obtained:

$$B_n = I_o \cdot e^{\left(-\delta_{cda} \cdot T_{Lam2} \cdot AM\right)}$$

T_{Lam2} is evaluated for $AM = 2$ and its correspondence with *aod* is also indicated on the graph. Any important deviation between the predicted and measured clear-sky values indicates calibration uncertainties, pyrheliometer misalignment, soiled or shaded sensors, or miscategorization of clear-sky conditions.

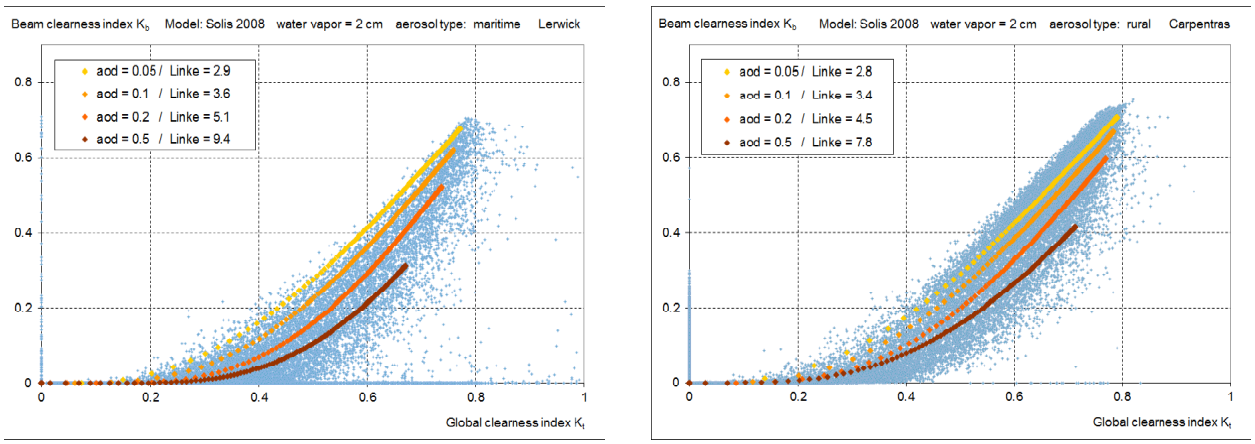

Figure 8 The beam clearness index is plotted against the global clearness index for Lerwick (maritime) and Carpentras (rural). On the same graph, clear sky modelled values are represented for 4 different aerosol loads. The corresponding Linke turbidity coefficients are also indicated

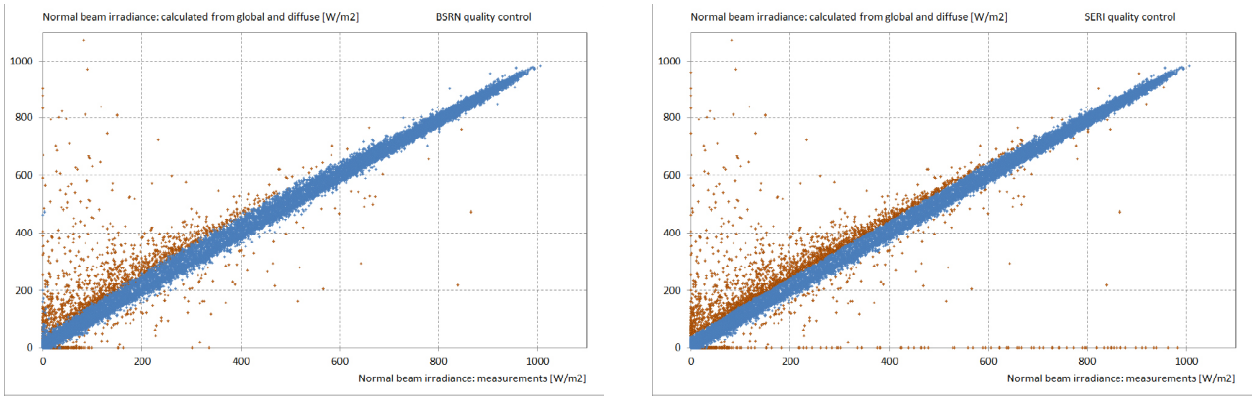

Figure 9 Quality control applied on the beam irradiance when the three components are available. The selected hourly values are represented in blue. For the QC applied in this report, the limit is also reported on the graph.

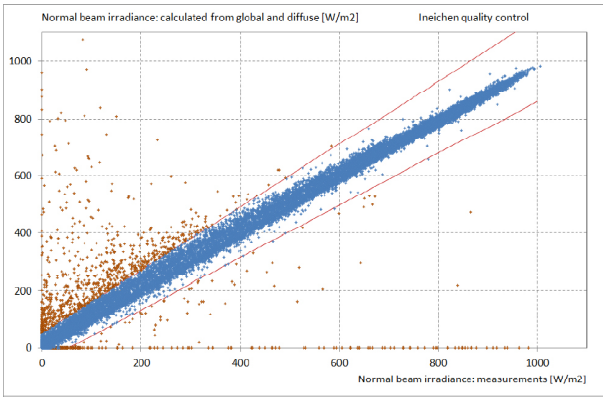

When the three components, global, diffuse and beam, are available, the closure equation can be applied. Due to the measurement methods for each of the components, the strict equality cannot be verified for all the values and acceptability limits are to be defined. For example:

- the BSRN quality control is the following:

$$\frac{G_h}{\left[D_h + B_n \sin(h)\right]}$$ should be within 8% for $h > 15°$ and 15% for $h \le 15°$

for $$D_h + B_n \sin(h) > 50 \left[\frac{W}{m^2}\right]$$

- the SERI quality control for the closure is defined as follow

$$K_t = K_d + K_b \pm 0.03$$

- closure equation applied in this report:

if $$B_{ncalc} = \frac{G_h - D_h}{\sin(h)} \quad \text{and} \quad B_{limit} = 1.1 \cdot B_n + 50 \left[\frac{W}{m^2}\right]$$

then $B_n + \text{abs}(B_n - B_{ncalc}) < B_{limit}$

These different quality controls are illustrated in the Figure 9 where the selected hourly values are represented in blue.

6. Hourly, daily and monthly comparison indicators

6.1 First order statistics

The most conventional comparison indicators are the mean bias difference (*mbd*), the root mean square difference (*rmsd*), the standard deviation (*sd*) and the determination coefficient (*R*); they represent a quantification of the model dispersion and are defined as follow:

$$mbd = \frac{\sum\left(G_{sat} - G_{mes}\right)}{N} \qquad rmsd = \sqrt{\frac{\sum\left(G_{sat} - G_{mes}\right)^2}{N}}$$

$$sd = \sqrt{\frac{\sum\left(G_{sat} - \overline{G_{mes}}\right)^2}{N}} \qquad R = \frac{\sum\left(G_{sat} - \overline{G_{sat}}\right) \cdot \left(G_{mes} - \overline{G_{mes}}\right)}{\sqrt{\left(\sum\left(G_{sat} - \overline{G_{sat}}\right)^2\right) \cdot \left(\sum\left(G_{mes} - \overline{G_{mes}}\right)^2\right)}}$$

where G_{mes} and G_{sat} represent respectively the measured and the modeled irradiance. The *mbd* gives an indication of the systematic bias of a model. Even if the average bias over all the sites is small, it can be highly variable from one site to the other. Therefore, the standard deviation of the biases (bias standard deviation *bsd*) is evaluated, it give an indication of the spatial stability of the model.

Comparison can also be done in terms of frequency of occurrence and cumulated frequency of occurrence: for the irradiance, it gives an indication of the repartition for each level of radiation, and for the clearness index, it assess that the modeled level of radiation occurs at the right time during the day. The obtained graph is a line (or a bar chart) representative of the relative frequency of occurrence of the considered parameter. This is illustrated on Figure 10 (left) for the clearness index K_t. On the same graph, the frequency of occurrence of the ground measurements is represented as grey bars, and the different models in color lines.

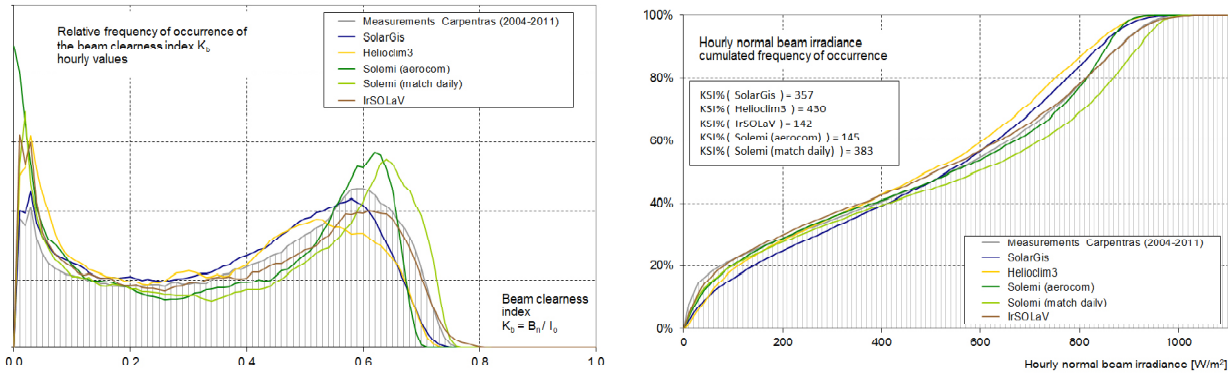

Figure 10 Relative frequency of occurrence of the clearness index (left) and the cumulated frequency of occurrence of the beam irradiance for the measurements (grey) and the different models (right).

6.2 Second order statistics

A second order statistic, the Kolmogorov-Smirnov test (Massey 1951, Espinar 2009), is also applied to the data. It represents the capability of the model to reproduce the frequency of occurrence at each of the irradiance level. In order to avoid a peak at the zero level of the beam irradiance, these values are excluded from the statistic. A visualization is given on Figure 10 (right) where the irradiance cumulated frequency of occurrence is represented against the irradiance for the same site than above. The quantitative value representative of the Kolmogorov Smirnov test Integral (*KSI*) is defined as:

$$KSI = \int_{G_{\min}}^{G_{\max}} \left| F_c\left(G_{sat}\right) - F_c\left(G_{mes}\right) \right| \cdot dG_{mes}$$

where $F_c(G_{mes})$ and $F_c(G_{sat})$ are respectively the irradiance ground measurements and the corresponding modelled cumulated frequencies of occurrence. *KSI%* is then obtained by normalizing *KSI* by a critical value depending on the number of events.

These statistical parameters include dispersions introduced by:

- the retrieval procedure,
- the comparison of point measurements (ground data) with area measurements (pixels),
- the comparison of the average of four instantaneous measurements with 60 minutes integrated values.

6.3 Model-measurements difference distribution

In terms of validation, when evaluating satellite derived parameters with the same time step, the comparison can be done by means of scatter plots; these give a visual evaluation of the capability of the model to reproduce the measurements. On these graphs, the diagonal line is representative of an ideal model, and the points should lay around this line. An illustration is given on Figure 11 for hourly and daily values.

On Figure 12, the distribution of the difference between the model and the

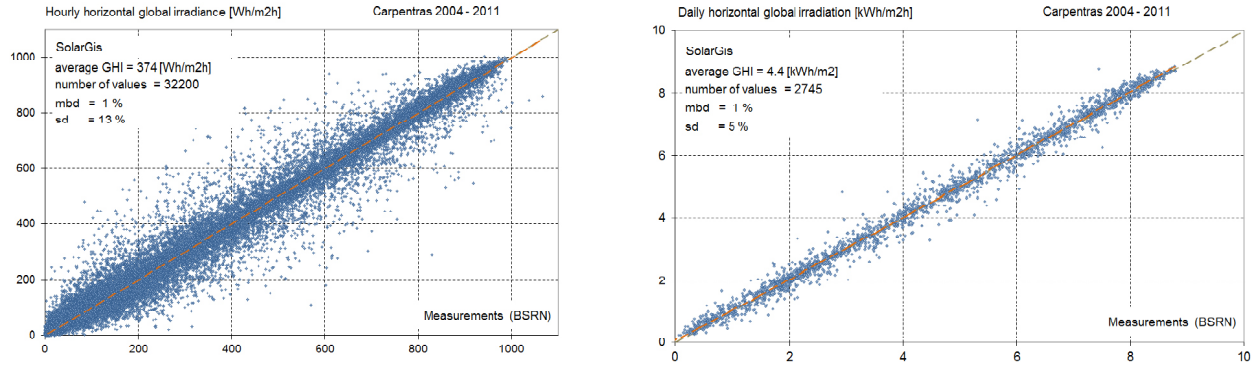

Figure 11 Hourly and daily modelled against measured global irradiance at the site of Carpentras for the whole considered period.

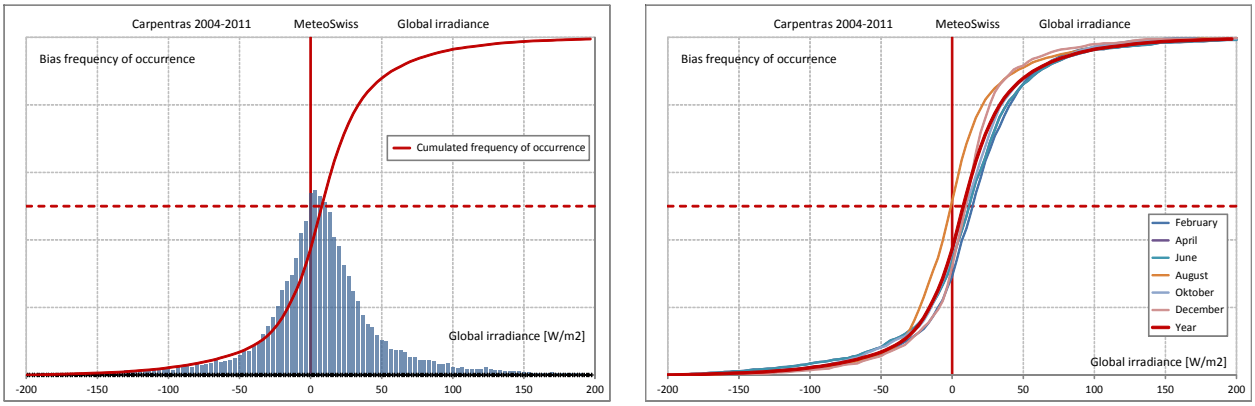

Figure 12 Difference distribution (left) between model and measurements for the MeteoSwiss model and the site of Carpentras. On the right graph, the cumulated frequency of occurrence is given for 6 months, MeteoSwiss model and Carpentras site.

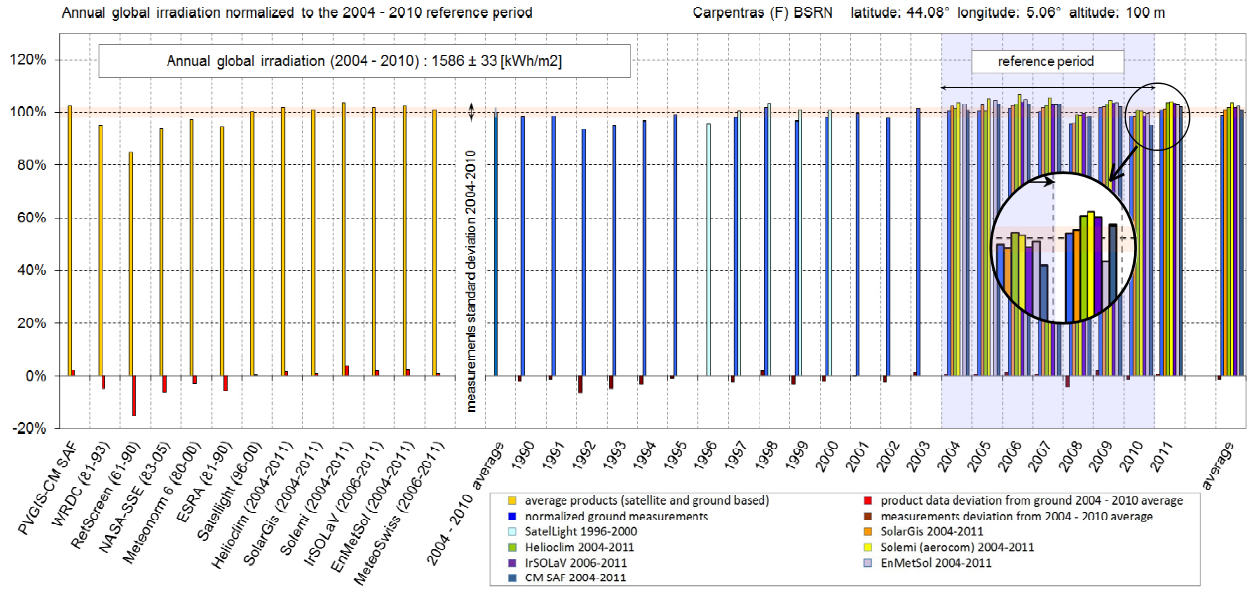

Figure 13 Total annual irradiation normalized to the average annual value over the reference period (2004-2010) for the site of Carpentras.

measurements around the 1:1 axis for hourly values is represented in term of frequency of occurrence for the whole period, and, in the Annex, for the months of April and August. On the same graph, the cumulated frequency of occurrence is also represented. For a good result, this curve should be as steep as possible, and cross the 50% value on the zero axis of the horizontal scale. The cumulated frequency is given every two months on a separate graph (Figure 12, right). The same representations are done for the three radiation components.

7. Interannual variability analysis method

The annual global and beam irradiation values are analyzed year by year. A reference period covering the years 2004 to 2010 will guide the evaluation of the different products. The yearly total determined by the average over this reference period is used as normalization value for all the annual totals. This normalized average (= 100%) is represented on the Figure 13 by the first blue bar from the left and labelled *2004-2010 average*. A standard deviation is calculated over the 8 years reference period, it is represented on the graph by the light orange zone surrounding the 100% line.

The following values are represented on Figure 13:

- the year per year annual ground irradiation measurements are represented by blue bars,
- the average or typical data banks, satellite based or ground measurements, are represented by the yellow bars on the left part of the graph,
- the year per year SolarGis data are represented by the orange bars,
- the year per year Helioclim 3 data are represented by the green bars,
- the year per year Solemi data are represented by the light yellow bars,
- the year per year IrSOLaV data are represented by the dark violet bars,
- the year per year CM-SAF data are represented by the light violet bars,
- the year per year MeteoSwiss data are represented by the dark blue bars,
- the year per year Satel-Light data are represented by the light blue bars for the years 1996 to 2000,
- the annual deviation from the 100% reference period average is represented by the red bars for the typical year data,
- the ground measurements annual deviation from the reference period are represented by the brown bars.

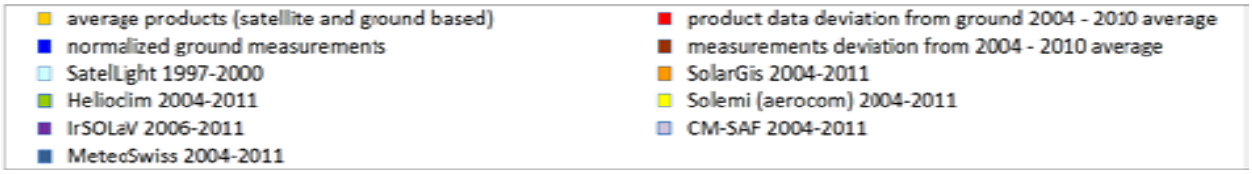

This method implies that there are no missing values in the evaluation of the yearly total. As this is not always the case, and to circumvent the elimination of too many data, a correction has to be applied as described in section 8.4.

8. Ground data validity assessment, calibration and stability

The first step in a model validation procedure is to assess the validity of the ground measurements. This can be done by applying a stringent quality control, but if some simple errors like a time shift in the data can be corrected, the suspicious data should be discarded. After having confirmed the time step in the data banks, the following tests are applied on the time series.

8.1 Comparison with Aeronet network

For 6 of the 18 ground measurements sites, data from a nearby Aeronet station are used to assess the calibration coefficient of the instruments. These are Carpentras (France), Davos (Switzerland), Madrid (Spain, only for 2012), Sede Boqer (Israel), Tamanrasset (Algeria) and Toravere (Estonia). The Solis clear sky model (Müller 2004, Ineichen 2008) is used to evaluate the global and beam irradiance from the aerosol optical depth *aod* and the water vapor content *w* of the atmosphere.

To validate the calibration coefficient applied during the measurements, the clear sky values are selected from the measured data (see section 5.2), and compared with the corresponding values derived from the Aeronet data and the Solis model.

For all the sites except Davos, Table II shows small differences between the sets of data, less than 2% in the average, these effects are not significative enough to consider a calibration adaptation (see for example, Figure 7 for the site of Carpentras).

The site of Davos shows differences of the order of 5% between spring and autumn, probably due to snow effects.

8.2 Long term stability

For the long term stability test, one can assume that the highest global and beam irradiance values do not vary significantly from one year to the other, and that a steep variation should be an issue of a calibration drift, more particularly when the effect disappears abruptly, i.e. in the case of a re-calibration of the sensors.

The long term stability is verified by comparing year by year the highest values of the hourly global and beam irradiance (see Figure 7). This analysis pointed out some significative drifts given in Table II for the following data:

- Davos: the beam irradiance is 20% too high from December 1999 to February 2000. This period is not included in the validation, but is integrated in the interannual variability analysis,
- Vaulx-en-Velin: the irradiance is 5% to 9% too high from 1995 to 2004,

- Zilani: the global irradiance is 10% too low in 1999, and the beam is 15% too high in 2000. Here also, it is not included in the validation period.

After applying the corresponding coefficients on the data, the quality control show normal behavior.

8.3 Components coherence

The component coherence is verified according to section 5.3 with the help of the closure equation when the three components are available. The results of the coherence test are given in Table II in term of a percentage of data kept after the test. This percentage stays between 68% and 93%.

The lowest value, 68%, is the result for Davos, where the beam component is not

Site	year per year comparison		aeronet comparison	Remark	Closure	Interannual	
	global irradiance	beam irradiance	G_h and B_n		equation	Gh	Bn
Almeria (Spain)	2001-2011	2001-2011	n/a	none	93%	100%	100%
Bratislava (Slovakia)	1994-2007	1994-2007	n/a	none	n/a	100%	100%
Carpentras (France)	1995-2011	1995-2011	2003-2011	G_h(aero/solis) > G_h(bsrn) [around 2%] Gh(aero/cpcr2) ≈ Gh(bsrn)	83%	99%	98%
Davos (Switzerland)	1999-2011	1999-2011	2006-2011	Bn 20% to high from Dec. 1999 to Feb 2000 Aeronet Gh 5% higher in spring than in autumn	68%	91%	97%
Geneva (Switzerland)	1995-2011	1995-2011	n/a	Gh compatible with Payerne and Vaulx-en-Velin	n/a	99%	94%
Kassel (Germany)	2003-2011	2003-2011	n/a	none	91%	98%	98%
Lerwick (Great Britain)	2001-2009	2001-2009	n/a	none	98%	94%	89%
Lindenberg (Germany)	1995-2006	1995-2006	n/a	none	91%	100%	100%
Madrid (Spain)	2004-2011	2004-2011	2012	Gh and Bn within 2-3% with aeronet Bn: too many missing data for interannual validation	84%	99%	86%
Nantes (France)	1995-2010	1995-2010	n/a	none	n/a	97%	94%
Payerne (Switzerland)	1994-2009	1994-2009	n/a	Gh compatible with Geneva	81%	100%	97%
Sede Boqer (Israel)	2003-2011	2003-2011	1996-2010	Bn(aero)<Bn(bsrn) [2% summer] Gh 2% to high from 2005-2008	90%	100%	94%
Tamanrasset (Algeria)	1995-2010	1995-2010	2006-2009	Gh, very clear conditions, at noon, 5% underestimation by aeronet/solis 1% overestimation by aeronet/cpcr2	90%	100%	99%
Toravere (Estonia)	1999-2011	1999-2011	2002-2009	none	88%	100%	98%
Valentia (Ireland)	1996-2009	1996-2009	n/a	none	n/a	97%	94%
Vaulx-en-Velin (France)	1995-2011	1995-2011	n/a	1995-2004 Gh and Bn to high (5-9%)	90%	96%	95%
Wien (Austria)	1994-2010	1994-2010	n/a	none	n/a	100%	97%
Zilani (Letonia)	1993-2009	1993-2009	n/a	Gh 10% to low in 1999 Gh 15% to high in 2003	91%	99%	98%

Table II List of the ground sites with year by year period of comparison, the aeronet convergent period, the results of the closure test, and the percentage of aqcuired monthly values considered for the interannual variability.

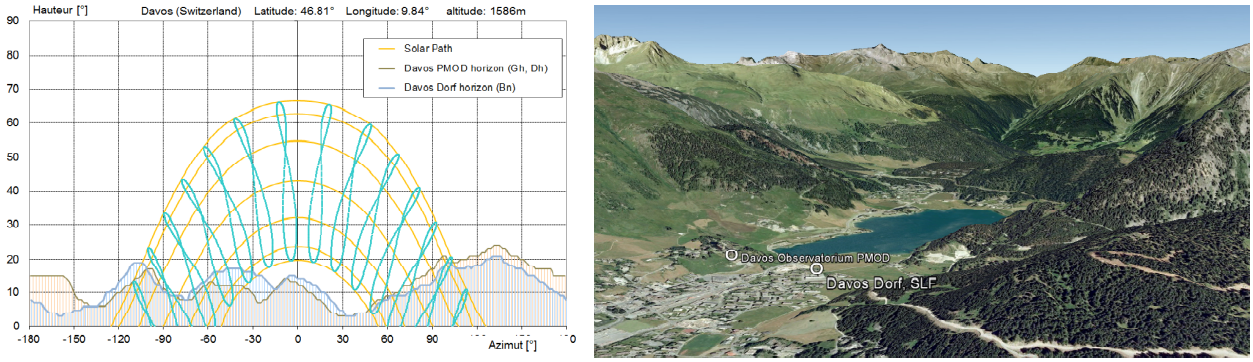

Figure 14 Horizon of the two sites of Davos PMOD and Davos SLF. The sky view factors do not differ, but slight differences can occur on the beam component.

acquired in the same location than the global and the diffuse; a slight difference in the time stamp is also possible. In addition, the distance between two sites is about 300 meters, Davos is in a valley and the two horizons are slightly different as shown on Figure 14. If the effect on the global irradiance is not visible, the sky view factors are similar, the beam component can be influenced by this difference.

The closure equation is applied on the normal beam component which is very sensitive for low solar elevations, and therefore, values of 90% are satisfactory.

The site of Leerwick shows a 98% even if the three components are stamped as separate measurements at the WRDC server. It is probable that the third component is retrieved from the two others.

For the sites where only two components are available, the closure equation is not applicable, and 100% of the data are kept.

The second coherence test is done on only the global and the beam component by comparing the corresponding clearness indices (Figure 8 in section 5.3). This test is applied indifferently on beam measurements, or beam evaluated from global and diffuse irradiances. For this test, only two sites show singularities:

- as shown on Figure 15, the beam clearness index in Lerwick (A) shows values that seems too low compared with the clear sky model Solis which is also represented on the figure for four different aerosol optical depths. For comparison, the same graph is given for the site of Almeria (B). This is confirmed with the diffuse fraction test given on (C) where the fraction is high compared to the clear sky model. This test is applied on only the global and the diffuse components and is independent from the beam. This can be a result of very high permanent turbidity. The closure test is coherent.
- for the site of Madrid, the shape of Figure 16E is not common, it is the only site showing such a behavior. Replacing the beam component in the clearness index by the global/diffuse difference improves slightly the shape, but it is still not common (F). Another issue can be a levelling default of the global sensor. A sensitivity test is conducted on the data of Almeria and given on Figure 16. The reference graphs drawn from the measurements are given in (A and B). When an levelling error of 3° is artificially introduced in the measurements, the result given on (C and D) show a similar behavior compared to the corresponding graphs for Madrid (E and F). This could be an explanation of this singularity.

8.4 Data validation for the interannual variability

The aim of the analysis of the interannual variability is to take into account the natural variation of the irradiation from one year to the other in the model uncertainty. To conduct a significant interannual variability analysis, a long period of data is needed.

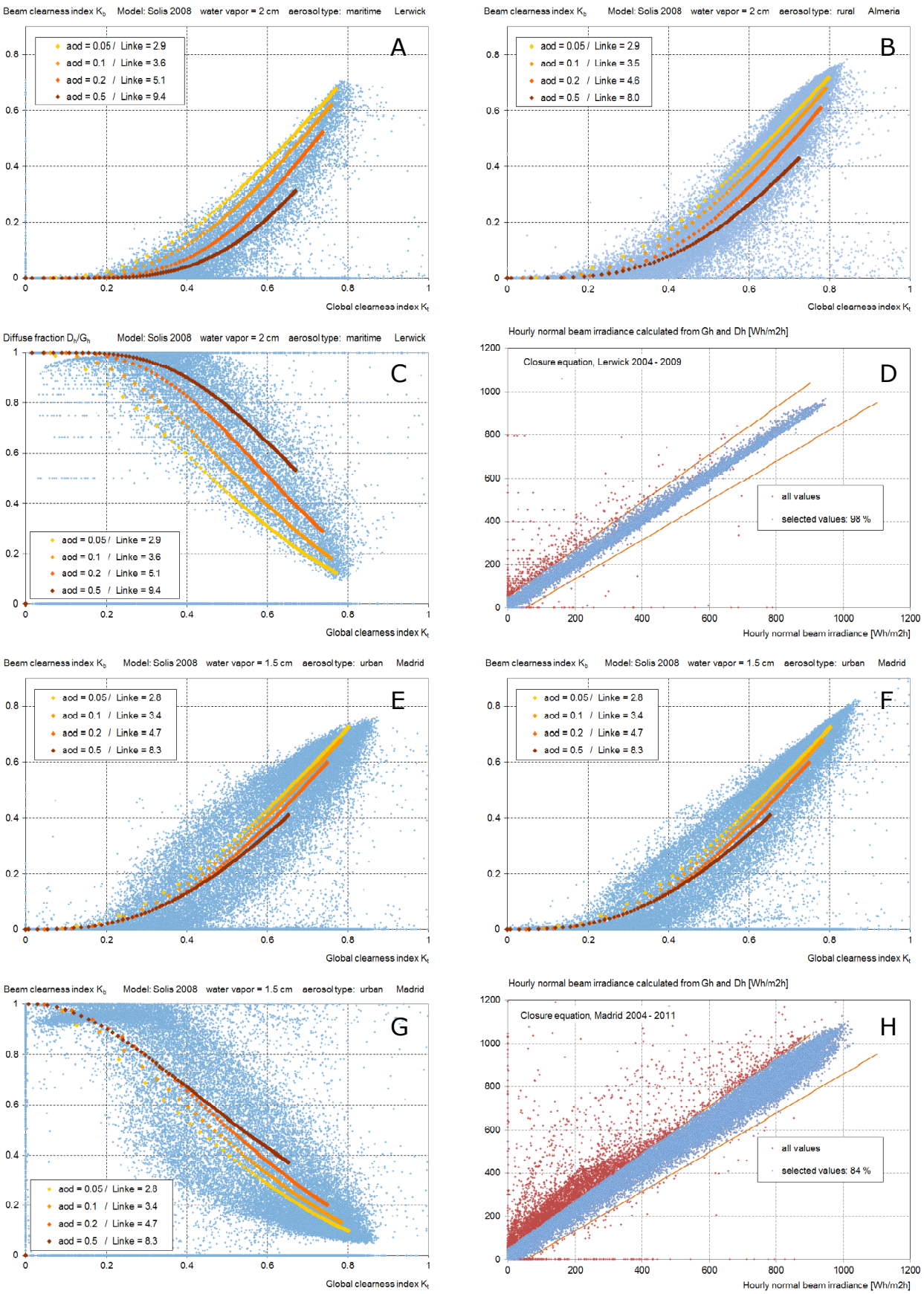

Figure 15 Components coherence test. Site of Lerwick: (A) K_b versus K_t, low beam component compared to the Solis clear sky, (C) diffuse fraction versus K_t, high diffuse. The closure equation (D) gives good results. (B) Almeria is given for comparison purpose.
(E to G) Site of Madrid: (E and G) it is the only site with these specific shapes. Slight improvement when representing the beam evaluated from the global and the diffuse (F). The closure equation (H) shows high discrepances.

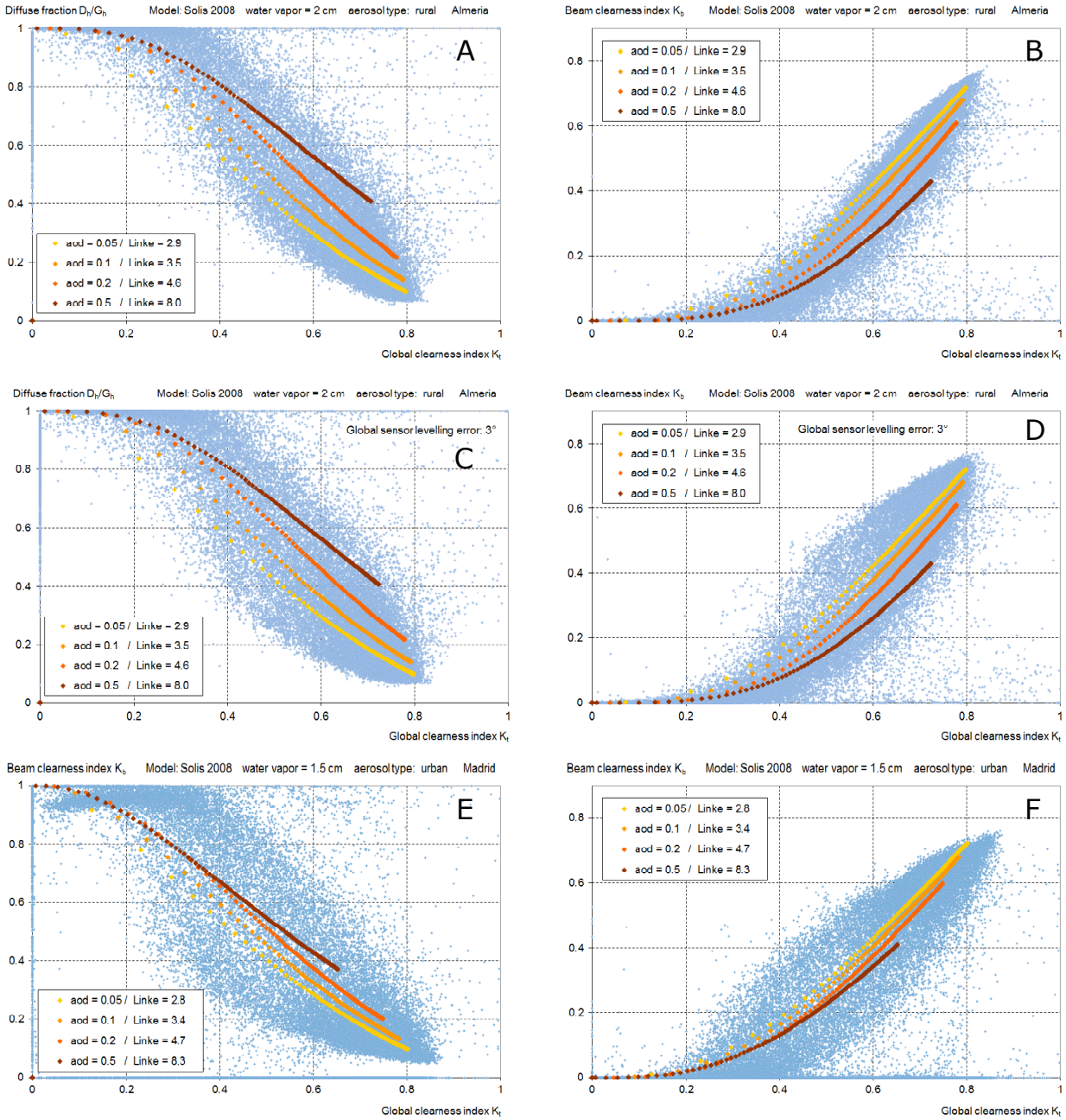

Figure 16 Components coherence test. Global sensor levelling sensitivity study on the data from Almeria. (A and B) Diffuse fraction and clearness index tests applied on the measurements. (C and D) effect on the tests for a 3° sloped global sensor. The shape on (D) looks similar to (F).

These long time series have to be continuous and with no missing data. As the majority of the ground measurements time series are not complete and as it is not possible the fill the gaps, a strategy has to be developed to circumvent the problem.

The following corrections are applied on the data: to obtain a yearly total, the data are taken month by month and added. For each month, the missing share of ground measurements is evaluated in term of a number of missing data percentage. When the gaps' length represents less than 5% of the month, a linear extrapolation is applied on the monthly values based on the normalized number of hourly values aggregated in the considered month. When more than 5% of the data are missing, the monthly value is replaced by the average of all the corresponding months of the

considered time series. The missing share statistics are given in Table II.

In Lerwick, the 11% missing data for the beam component occur mainly in 2011. For the site of Madrid too many data are missing for the beam component, so that the interannual variability analysis is not significative.

Due to these corrections, the results given in the interannual variability bar charts do not correspond exactly to the hourly validation results. As the hourly comparison is restricted to validated values, some differences may also occur depending on the length of the comparison period. Nevertheless, the results are significative when considered as a general overview of the tendency of a model to reproduce the data.

9. Validation results

9.1 Hourly, daily and monthly validation

The total amount of points included in the comparison and the corresponding irradiance and irradiation averages are the following:

- 475'000 hourly values G_h = 340 B_n = 350 D_h = 135 [W/m²]
- 43'000 daily values G_h = 3.7 B_n = 3.8 D_h = 1.45 [Wh/m².day]
- 1'700 monthly values G_h = 110 B_n = 110 D_h = 43 [Wh/m².month]

The number of ground or satellite derived values differ from one site to the other, and the covered periods are not of the same length for all the sites (see Table II).

Table III and Figure 17 give the main results of the validation (the complete results, site by site, model by model, component by component, in hourly, daily and monthly vues, and in absolute and relative values are given in the annex, Tables a-I*n*, a-II*n* and a-III*n*, *n*=g, b or d for global, beam or diffuse). A general observation is that the

	SolarGis						Helioclim 3					
	Gh		Bn		Dh		Gh		Bn		Dh	
	mbd	sd	mbd	sd	mbd	sd	mbd	sd	mbd	sd	mbd	sd
hourly [Wh/m2h]	341		351		134		345		354		134	
	0	57	-6	119	7	47	5	70	21	166	-13	60
	0%	17%	-2%	34%	5%	35%	1%	20%	6%	47%	-10%	45%
Daily [kWh/m2]	3.73		3.83		1.46		3.81		3.91		1.49	
	0.00	0.29	-0.05	0.75	0.07	0.32	0.05	0.44	0.22	1.25	-0.14	0.46
	0%	8%	-1%	20%	5%	22%	1%	12%	6%	32%	-9%	31%
Monthly [kWh/m2]	108.5		111.4		42.5		109.3		112.1		42.8	
	-0.1	3.6	-1.7	10.4	2.3	4.5	1.5	7.5	6.6	18.6	-4.1	6.1
	0%	3%	-2%	9%	5%	11%	1%	7%	6%	17%	-10%	14%
bias sd	2.1%		5.9%		7.5%		5.1%		13.9%		14.2%	

	Solemi						Heliomont					
	Gh		Bn		Dh		Gh		Bn		Dh	
	mbd	sd	mbd	sd	mbd	sd	mbd	sd	mbd	sd	mbd	sd
hourly [Wh/m2h]	342		350		134		340		354		135	
	6	80	-40	170	33	80	4	66	0	140	5	55
	2%	23%	-11%	49%	25%	60%	1%	19%	0%	39%	4%	41%
Daily [kWh/m2]	3.73		3.82		1.46		3.75		3.85		1.47	
	0.07	0.49	-0.39	1.23	0.33	0.62	0.04	0.33	0.02	0.90	0.05	0.39
	2%	13%	-10%	32%	23%	42%	1%	9%	0%	23%	3%	27%
Monthly [kWh/m2]	108.8		111.3		42.3		107.6		110.3		42.1	
	2.0	6.2	-12.6	10.6	10.5	9.6	1.1	4.2	0.3	12.1	1.6	5.2
	2%	6%	-11%	15%	25%	23%	1%	4%	0%	11%	4%	12%
bias sd	4.8%		14.5%		25.2%		3.6%		9.3%		9.6%	

	CM SAF						IrSOLaV					
	Gh		Bn		Dh		Gh		Bn		Dh	
	mbd	sd	mbd	sd	mbd	sd	mbd	sd	mbd	sd	mbd	sd
hourly [Wh/m2h]	337		354		131		340		353		134	
	0	75	7	165	2	55	2	81	-1	174	5	62
	0%	22%	2%	47%	2%	42%	1%	24%	0%	49%	4%	46%
Daily [kWh/m2]	3.56		3.73		1.38		3.60		3.73		1.41	
	0.00	0.43	0.07	1.10	0.03	0.39	0.02	0.44	0.00	1.17	0.04	0.41
	0%	12%	2%	30%	2%	28%	0%	12%	0%	31%	3%	30%
Monthly [kWh/m2]	104.2		109.4		40.5		104.3		107.9		40.8	
	0.1	5.0	2.0	11.7	0.8	4.8	0.6	6.4	-0.3	13.8	1.6	5.3
	0%	5%	2%	11%	2%	12%	1%	6%	0%	15%	4%	13%
bias sd	3.7%		9.1%		8.3%		4.2%		12.0%		13.8%	

Table III Results of the hourly, daily and monthly validation. The standard deviation calculated on the mean bias differences over all the 18 sites.

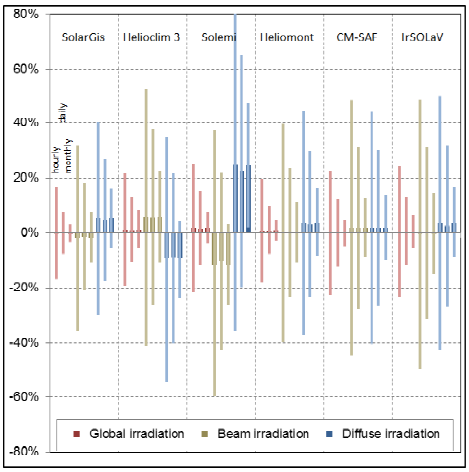

Figure 17 Corresponding graphical representation of the results.

hourly global irradiance is retrieved with a negligible bias and a standard deviation ranging from 17% to 24% (57 to 81[W/m²]), the beam component from 34% to 49% (119 to 174[W/m²]) with a -11% to +6% bias, and the diffuse from 35% to 60% (46 to 80 [W/m²]) with a bias from -10% to +25%. If the overall bias for the global irradiance models is near of zero, it can be highly variable from one site to the other. This is highlighted by the standard deviation of the mean bias deviation *bsd*; it varies from 2.1% to 5.1% for the global component. For the beam component (and a fortiori for the diffuse irradiance), the bias varies from site to site and model to model. It has to be noted that the beam irradiance bias for Solemi is always negative (opposite bias for the diffuse component, see Table a-Ib to a-IIIb and a-Id to a-IIId).

For the CM-SAF algorithm, when representing the bias versus time, a similar moreless important pattern can be seen for all the sites during the summer 2006 and 2008. This pattern is illustrated on Figure 18a and 18c for Carpentras and Sede Boqer. On the graphs b and d, the corresponding clearness index is represented in yellow for the measurements and in blue for the model. It shows that the underestimation is not due to specific or extreme meteorological conditions. The aerosol optical depth *aod* and the Linke turbidity T_L retrieved from the ground normal beam irradiance are also

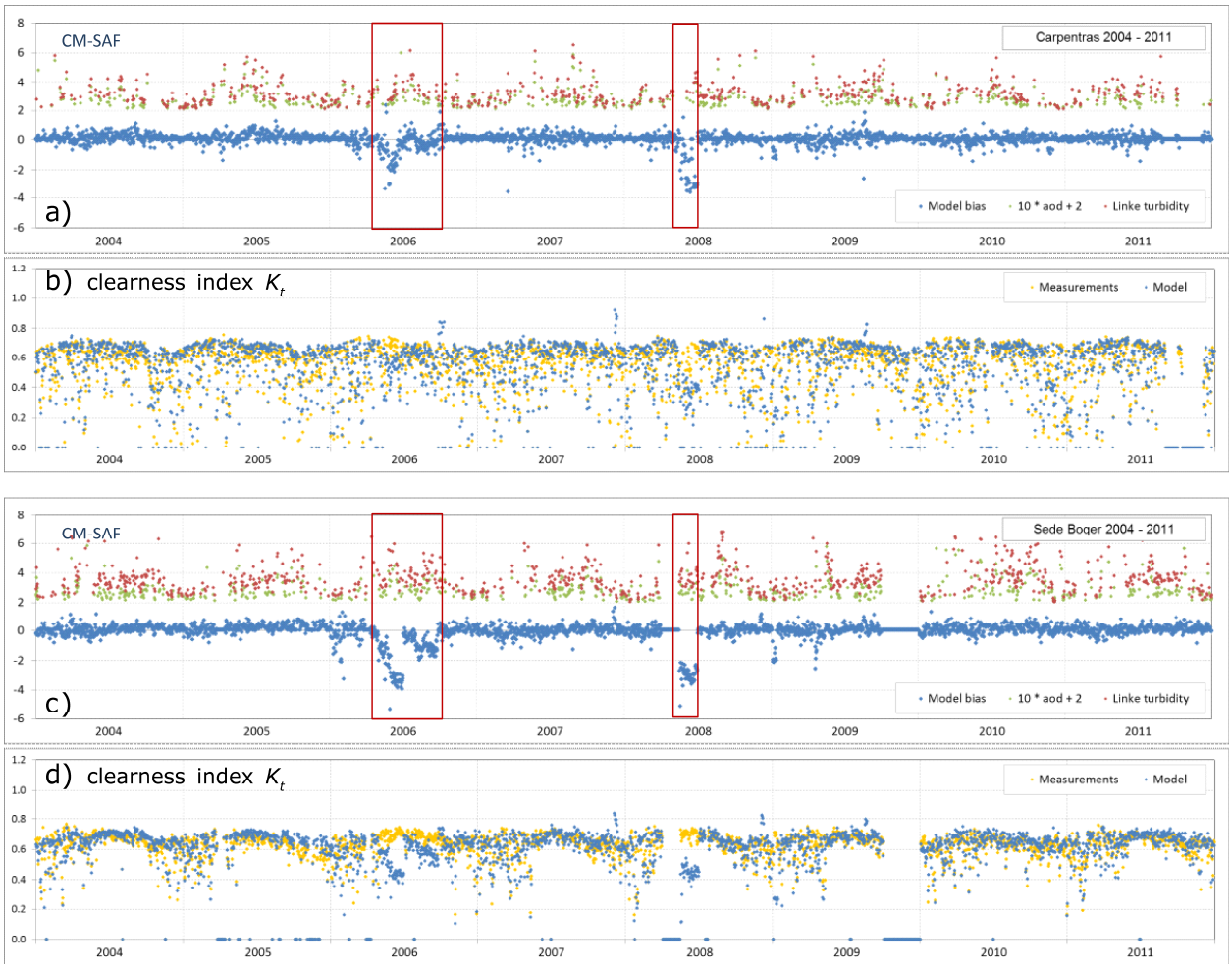

Figure 18 Daily model-measurements bias (blue dots) for the sites of Carpentras and Sede Boqer (a & c). On graph b) and d), the modelled (in blue) and measured (in yellow) clearness index are representd.

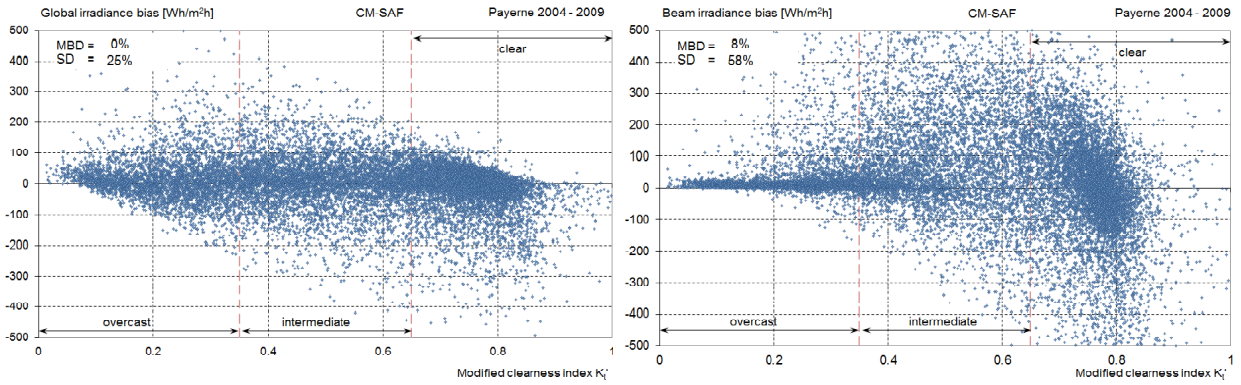

Figure 19 Model bias versus the clearness K_t (or sky conditions) for the the global and beam components.

represented on the graphs. The undersetimation during these two periods cannot be explained by extreme polluted episodes. On the other hand, these patterns are not present on the other models' results. As it seems that this is an unexplained problem that has to be solved, to not skew all the analysis, these two periods are removed from the validation for the CM-SAF model and all the sites.

In a general way, for the global component and all the models, the bias distribution around the 1:1 axis follows a un- or slightly skewed normal distribution, so that the standard deviation indicator is significative (see Figures 11 & 12, a-1g to a-8g). This is not the case for the normal beam irradiance bias, where bimodal, skewed or not normal distributions can occur depending on the model and the site. No common rule can be drawn from the Figures a-1b to a-8b, the shape of the distribution depend on the clear sky model used and the specificities of the input parameters. For some sites with sunny conditions like Tamanrasset or Sede Boqer, the dispersion of the hourly bias is so high that the distribution cannot be considered as normal. In this case, the standard deviation has to be considered with precaution.

The observation of the bias versus the modified clearness index K_t' (or the sky type, see Figures a-9g and Fig. a-9b) shows the same general tendency for all the models and both components: a slight overestimation for cloudy conditions and an underestimation for clear skies. The highest effect is a beam component overestimation for intermediate conditions. This is illustrated on Figure 19. For clear conditions, the dispersion is due to an approximate knowledge of turbidity. In the case of intermediate cloud cover, the models do not identify with enough precision the type and thickness of the clouds.

The aerosol optical depth has the highest effect on the model uncertainty. To analyse its effect on the CM-SAF algorithm, a retro-evaluation of the *aod* is done on the ground measurements on a daily basis (Ineichen 2010). The bias is then represented versus the *aod* as illustrated on Figure 20. For almost all the sites, the bias is positively correlated with the aerosol optical depth. As expected, the effect is more pronounced for the beam component. To be sure that it is not an artefact issued by the retro-calculation, the aod is validated with aeronet data for the site of Carpentras as shown

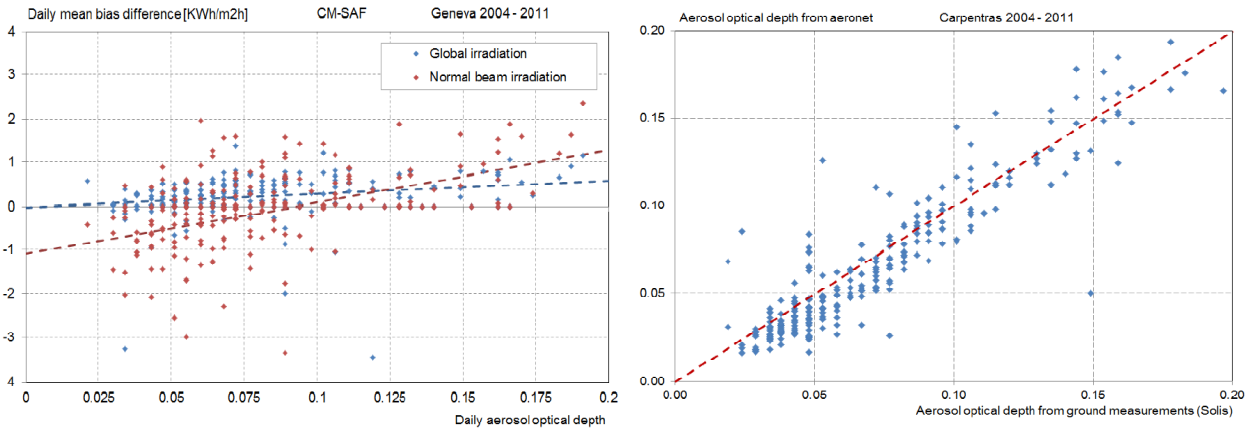

Figure 20 left: model bias versus the aerosol optical depth retrieved from the ground beam irradiance, right: validation of the retro-calculation method on the aeronet data from Carpentras.

on the right graph from Figure 20.

For the site of Davos, the snow cover during the winter period has a significant effect on all the models except SolarGis and Heliomont. If the snow cover is correctly taken into account by these two models, the other models show scatter plots with high dispersion for both the components. For the CM-SAF model, the snow effect is illustrated on Figure 21a and 21b, where the distribution of the differences is skewed

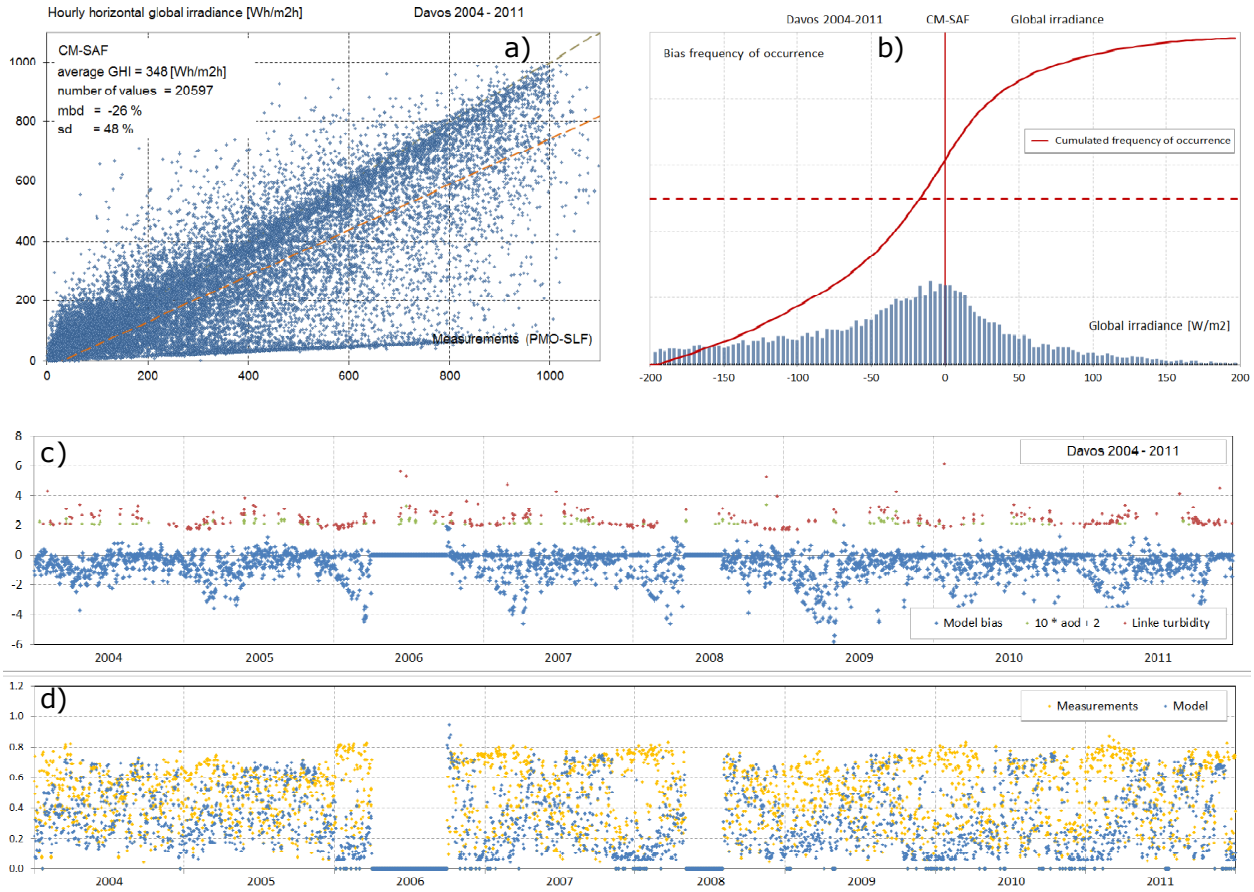

Figure 21 Illustration of the snow effect for the site of Davos and CM-SAF model. a) model-measurements scatter plot, b) distribution of the model-measurement differences around the 1:1 axis, c) daily model-measurements bias (blue dots) and d) modelled (in blue) and measured (in yellow) clearness index.

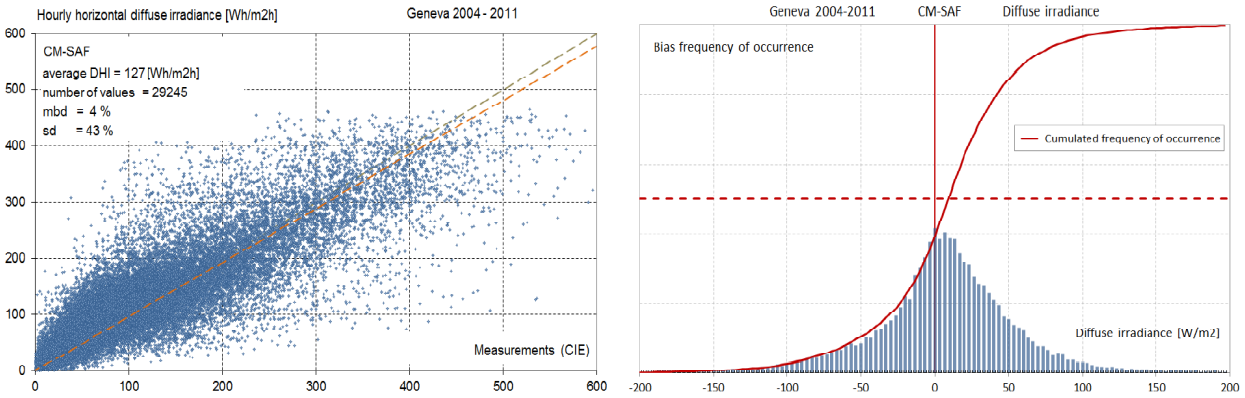

Figure 22 Diffuse irradiance scatter plot with the correspondig model-measurement difference distribution around the 1:1 axis.

to the left. On Figure 21c and 21d, the underestimation is visible for the snow period, i.e. from November to June. This period is removed from the Validation.

For the diffuse component, CM-SAF presents the lowest bias, and SolarGis the best precision. For these models, the distribution of the hourly bias present unskewed normal distributions as illustrated on Figure 22. This is an interesting option when diffuse irradiance is specifically needed, as for example when evaluating the UV erythema (Vernez 2013). The other models present often skewed distributions, sometimes not even normal distributions. For example, the results for Solemi on sunny sites like Sede Boqer, Tamanrasset and Almeria (see Figures a-1d) show a high dispersion, probably in correlation with the use of low time and space resolution climatological data banks for the *aod* and *w*.

Figure 23 is a graphical illustration of the monthly validation. On the left graph, monthly values surrounded by ± one standard deviation for the CM-SAF model and the measurements are represented. On the right graph, all the nowcasting models are shown; the measurements are in red, the dashed red lines represent ± one standard deviation around the monthly value.

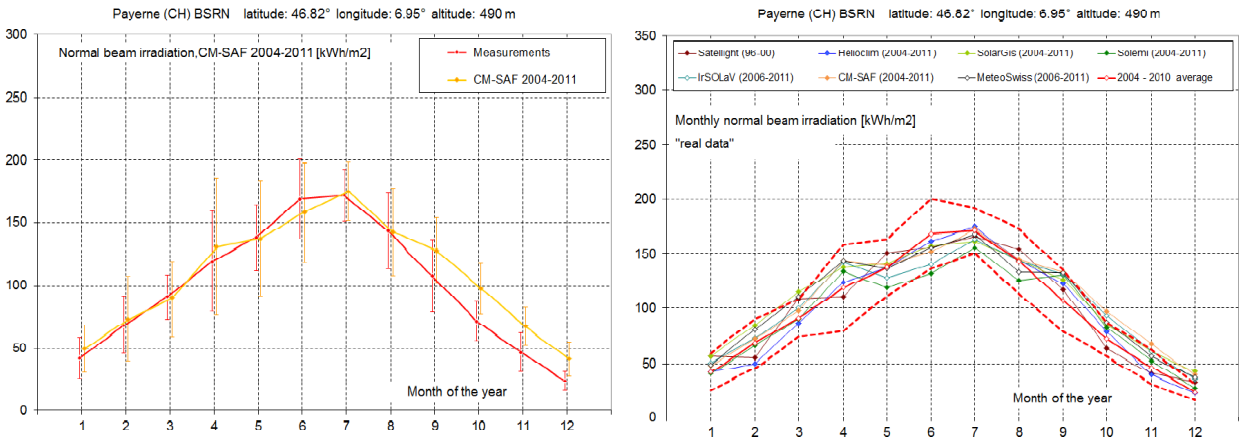

Figure 23 Left: monthly values surrounded by ± one standard deviation for the CM-SAF model. Right: monthly values for all the models. In red, the measurements, the red dashed lines represent ± one standard deviation.

Figures a-11, a-18 and a-19 in the annex give a graphical representation for all the sites and models. For the global component, and for either the average or the nowcasting models, 94% of the monthly modeled values are situated between the two dashed lines. For the beam component and the average models, 83% of the values are between the dashed lines, and for the nowcasting models, the 88% of the monthly values are within ± one standard deviation limits. Except for Madrid where all the models present a significative positive bias for the spring months, no particular pattern can be pointed out, the deviation depend on the model and the site.

9.2 Frequency distribution

The correspondence between the frequency distribution of the modeled values and the measurements is as important as a low bias and standard deviation. It is the guaranteeing of a realist representation of the solar ressource by the satellite models. The general observation is that all the models for all the sites have a coherent frequency distribution representation of the global irradiance level (with the exception of Davos for the snow periods, Figures a-12g and a-13g). This is not the case when considering the global clearness index frequency distribution. For sites with high insolation levels like Madrid, Sede Boqer and Tamanrasset, the number of occurrence for high clearness indices is overestimated (Figures a-14g and a-15g).

For the beam component, the frequency distributions, for both the irradiance/irradiation and the clear sky index are more randomly distributed, depending on the site and the model, without specific patterns. The only thing which one can point out is higher discrepancy with the measurements for sunny sites such as Sede Boqer or Tamanrasset, and clear conditions. But here again, the bias is very different from one model to the other (see annex Figures a-14b and a-15b). An illustration is given on Figure 24 where the site of Tamanrasset is represented.

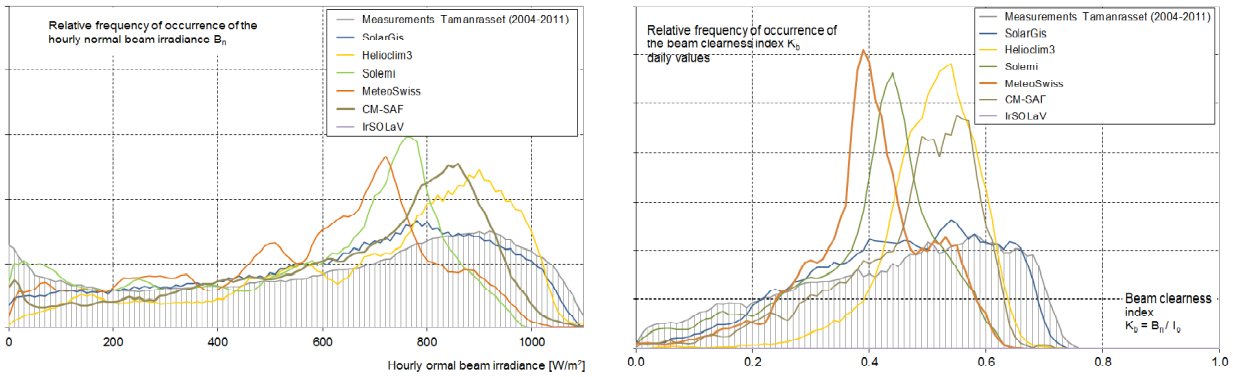

Figure 24 Frequency distribution of occurrence versus the hourly irradiance value and the beam clearness index for the site of Tamanrasset and all models.

9.3 Interannual variability

Beside the visual analysis of Figure a-20g and a-20b, it is interesting to compare the

	Yearly total [kWh/m2] average over 2004-2010	standard deviation over 2004-2010	PVGIS-CM SAF	WRDC (1981-1993)	RetScreen (1961-1990)	NASA-SSE (1983-2005)	MN 7 (1980-2000)	ESRA (1981-1990)	Satellight (1996-2000)	SolarGis (2004-2011)	Heliodim (2004-2011)	Solemi (2004-2011)	Heliomont (2006-2011)	CM-SAF (2004-2011)	IrSOLaV (2006-2011)	Yearly total [kWh/m2] average over 2004-2010	standard deviation over 2004-2010	NASA-SSE (1983-2005)	MN 7 (1980-2000)	Satellight (1996-2000)	SolarGis (2004-2011)	Heliodim (2004-2011)	Solemi (2004-2011)	Heliomont (2006-2011)	CM-SAF (2004-2011)	IrSOLaV (2006-2011)
Sites			Global irradiation, mean bias difference *mbd*															Beam irradiation, mean bias difference *mbd*								
Almeria	1850	2.5%	1.8%		-8.1%	-8.1%	-3.0%		4.9%	0.4%	6.1%	3.0%	3.2%	-0.1%	0.3%	2126	5.5%	-3.8%	-11.1%	15.1%	-1.9%	12.1%	-3.0%	6.3%	2.0%	-3.9%
Bratislava	1176	2.9%	3.2%	1.0%	1.1%	-1.0%	1.7%	4.3%	-3.5%	3.2%	-0.2%	5.4%	2.8%	6.5%	4.4%	1191	7.4%	-4.0%	-7.5%	-11.9%	-9.6%	-2.1%	-21.8%	-15.3%	3.5%	9.1%
Carpentras	1587	2.1%	2.5%	-4.8%	-15.0%	-6.0%	-2.8%	-5.4%	0.4%	0.3%	0.6%	2.7%	1.6%	2.1%	1.2%	1884	4.1%	0.4%	-10.1%	4.9%	-1.8%	-0.3%	-4.2%	3.0%	4.4%	-1.6%
Davos	1383	1.3%	-0.8%		-2.7%	-7.9%	2.1%	-2.9%	-17.5%	-4.2%	11.5%	-13.2%	-4.4%	-14.5%	-7.1%	1420	8.4%	-8.0%	18.1%	-26.2%	-2.8%	21.9%	-33.6%	-9.5%	-27.0%	-36.9%
Geneva	1282	2.3%	3.5%	-6.3%	0.1%	0.1%	-4.9%	-5.5%	-0.6%	4.2%	0.1%	6.4%	3.5%	4.1%	5.3%	1274	3.3%	4.3%	-9.8%	-0.9%	7.0%	1.9%	-4.2%	8.6%	9.4%	4.0%
Kassel	1048	2.7%	0.6%		-5.6%	-5.6%	-5.8%	-6.6%	-5.9%	-0.1%	-3.4%	0.8%	-2.9%	-1.4%	4.0%	874	6.4%	1.0%	-7.9%	-5.1%	2.0%	10.2%	-19.4%	-4.4%	7.4%	21.8%
Lerwick	810	4.7%		-4.3%	9.2%	9.1%	-3.5%	-4.4%	-2.5%	0.7%	5.4%	3.8%	-3.2%	-5.5%		580	13.3%	55.5%	18.2%	0.8%	6.9%	50.4%	-11.5%	21.6%	8.5%	
Lindenberg	1120	3.8%	-3.7%	-3.8%	-3.8%	-9.8%	-3.9%	-12.3%	-4.5%	-3.1%	-2.1%	-3.5%	-4.8%	-0.5%	-0.4%	1026	9.6%	-8.1%	1.4%	-0.4%	-6.4%	5.8%	-27.9%	-15.1%	2.6%	30.5%
Madrid	1697	4.9%	3.5%		-5.2%	-5.2%	-3.1%	-2.5%	1.7%	1.4%	4.4%	5.7%	5.6%	3.4%	1.9%	1798	5.2%	10.0%	-0.8%	14.1%	5.4%	8.6%	4.8%	16.4%	11.0%	-2.3%
Nantes	1266	3.4%	1.5%	-5.2%	-3.4%	-6.7%	-2.2%	-0.9%	-2.7%	-3.3%	0.4%	3.3%	0.7%	-0.2%	1.3%	1307	6.7%	-12.1%	-9.6%	-8.8%	-8.4%	2.7%	-11.1%	4.2%	0.6%	0.7%
Payerne	1278	2.4%	1.7%	-8.4%	-2.5%	0.4%	-1.9%	-8.3%	-2.8%	0.7%	-6.4%	1.8%	-0.1%	-0.3%	4.8%	1191	4.4%	11.1%	5.9%	2.0%	7.0%	-3.4%	-5.8%	6.1%	7.5%	12.5%
Sede Boqer	2114	1.2%	-9.2%	0.5%	-6.7%	-3.9%	-4.0%			0.6%	-6.1%	3.4%	4.7%	0.9%	-1.7%	2382	3.6%	4.6%	-5.4%		-4.6%	-16.9%	-8.7%	-3.1%	-4.8%	-7.8%
Tamanrasset	2345	1.8%	-2.8%	0.8%	2.6%	-8.1%	0.9%			-1.2%	2.1%	-1.8%	-1.0%	0.0%		2355	4.0%	6.1%	18.1%		2.5%	14.7%	-10.5%	-9.2%	6.3%	
Toravere	981	3.8%			3.1%	3.1%	-0.1%		4.6%	-2.3%	2.1%	-1.5%	-4.4%	-6.3%	-0.8%	1028	8.8%	8.4%	2.4%	7.2%	-6.5%	7.2%	-28.4%	-14.3%	-11.7%	1.9%
Valentia	1021	4.6%	9.4%	-3.9%	-4.8%	8.0%	-5.3%	-4.7%	-4.2%	-3.6%	4.1%	3.2%	1.8%	-5.1%	1.4%	992	13.4%	10.7%	-21.5%	-21.3%	-21.6%	3.3%	-25.1%	-2.3%	-20.1%	1.9%
Vaulx-en-Velin	1304	4.4%	3.4%	-7.8%	-4.0%	-3.0%	-6.3%	-3.3%	0.4%	3.1%	2.6%	7.3%	5.9%	5.0%	3.6%	1359	5.3%	-2.1%	-11.6%	-0.5%	-0.9%	4.2%	-4.7%	10.1%	7.9%	-0.5%
Wien	1175	2.7%	0.5%	-6.8%	-6.0%	-0.8%	1.0%	-7.0%	-1.4%	-0.3%	-3.0%	3.4%	0.4%	2.7%	0.7%	1112	8.0%	2.9%	-3.1%	-2.5%	-2.3%	4.0%	-12.7%	-3.5%	11.3%	15.0%
Zilani	1024	3.3%	-6.1%	-3.2%		2.5%	-2.6%		6.0%	-1.4%	10.9%	-3.2%	-2.6%	-5.9%	-17.6%	1000	9.1%	13.4%	-0.1%	20.5%	-0.2%	31.9%	-26.5%	-7.3%	-5.5%	-13.6%
All sites	1359	2.9%	0.1%	-3.5%	-3.5%	-3.3%	-2.3%	-4.5%	-1.6%	-0.1%	1.4%	1.8%	1.0%	0.1%	0.5%	1383	6.3%	3.8%	-1.6%	-0.1%	-1.6%	5.9%	-11.3%	0.1%	1.9%	-0.4%
All sites absolute mean bias			3.4%	4.0%	5.1%	5.1%	3.0%	5.1%	3.9%	1.7%	3.9%	3.9%	2.9%	2.7%	3.0%			7.5%	9.3%	9.5%	4.8%	10.0%	12.0%	7.8%	7.5%	7.8%
Standard deviation of *mbd*			4.6%	4.6%	6.5%	6.3%	3.4%	5.7%	5.9%	2.1%	5.1%	4.8%	3.6%	3.7%	4.2%			9.0%	11.9%	13.2%	5.9%	13.9%	14.5%	9.3%	9.1%	12.0%

mbd within one standard deviation | *mbd* within two standard deviations | *mbd* higher than two standard deviations

Table IV Results of the yearly validation and interannual variability analysis.

bias of the models with the interannual variability expressed by the standard deviation around the annual irradiation average for both the global and the beam components. The comparison results are given in Table IV. The blue columns represent the annual average for each site and the corresponding standard deviation over the reference period 2004-2010. The results for the different products are expressed as mean bias differences; if the *mbd* is less than one standard deviation *sd*, the cell background is represented in green. These *mbd* are highly variable from site to site and from model to model, even if the combined results for all sites are relatively good. On the last lines, the absolute bias and the standard deviation of the bias *bsd* is given for all models. These values express the spatial «smoothness» of the model.

From Table III, the following points can be underlined for the global component:

- the overall bias for PVGIS-CM SAF and Meteonorm 7 is situated within ± one standard deviation of the interannual variability, with a bias standard deviation *bsd* around 4%,
- all the nowcasting models have a low bias, within ± one standard deviation of the interannual variability. The *sbd* varies from 2.1% to 5.1% (Satellight covers not the same period and is given for comparison purpose),
- considering the site by site results, 60% of the site-model have a bias within ± one standard deviation of the interannual variability, 24% within ± two standard deviation, and 16% with a higher bias,

and for the beam component:

- the bias for NASA-SSE and Meteonorm 7 are within ± one standard deviation of the interannual variability with a *sbd* of respectively 9% and 12%,
- except Solemi, all the nowcasting models have an overall relatively low bias, within ± one standard deviation of the interannual variability. The corresponding *sbd* varies from 6% to 14%,

- considering the site by site results, 46% of the site-model have a bias within ± one standard deviation of the interannual variability, 29% within ± two standard deviation, and 25% with a higher bias.

10. Conclusions

The first conclusion is that the quality control is a key point in any model validation. Even if the data are highly qualified by the organization in charge of the acquisition, uncertainties can remain in the data and influence the validation. The best case is when independent data such as aerosol optical depth are also available.

The conclusions of the present study are the following:

- for latitude from 20° to 60°, altitude from sea level to 1600 m and various climate, the hourly global irradiance is retrieved with a negligible bias and an average standard deviation around 17% for the best algorithm. For the beam irradiance, the bias is around several percents, and the standard deviation around 34%,
- the standard deviation of the bias vary from 2% to 5% for the global irradiance, and from 6% to 14% for the beam component,
- as expected, the main dependence comes from the clear sky model and the knowledge of the aerosol optical depth. Better results are obtained with daily turbidity instead of climatic monthly values. A lower dependence with the atmospheric water vapor column and the solar elevation angle is pointed out,
- even if the snow cover is taken into account in the algorithm, the irradiance for sites situated in high altitude like Davos present a higher dispersion,
- for the majority of the sites, SolarGis, Heliomont and EnMetSol give the best statistics for all of the components.

11. Acknowledgements

The ground data were kindly provided by the Baseline Surface Radiation Network (BSRN), the Global Aerosol Watch project (GAW), the CIE International Daylight Measurements Program (Commission internationale de l'éclairage IDMP), the Centre Scientifique et Technique du Bâtiment (CSTB) in Nantes, the Universidad Politécnica de Madrid (UMP), the Ecole National des Travaux Publiques (ENTPE) of Lyon, the Deutsches Zentrum für Luft und Raumfahrt (DLR), the Frauenhofer Institute in Kassel (FhG), the Institute of Construction and Architecture of the Slovak Academy of Sciences, the Institut für Schnee- und Lawinenforschung (SLF) and the Physikalisch-Meteorologisches Observatorium Davos World Radiation (PMOD).

The satellite data were kindly provided by Geomodel Solar (Slovakia), MineParisTech and Transvalors SA (F), IrSOLaV (Spain), DWD: Deutcher Wetter Dienst (D), DLR:

Deutsches Zentrum für Luft und Raumfahrt (D), SatelLight server (F) and MeteoSwiss (CH).

A critical review of the quality control section was kindly carried out by Christian Gueymard.

12. Bibliography

Aeronet (AErosol RObotic NETwork) program, http://aeronet.gsfc.nasa.gov/.

Atwater M.A., Ball J.T. (1976) Comparison of radiation computations using observed and estimated precipitable water. J. Appl. Meteorol. 15, 1319-1320.

Beyer, H., Costanzo, C., Heinemann, D. (1996). Modifications of the HELIOSAT procedure for irradiance estimates from satellite images. Solar Energy, 56, 207- 21

Cano, D., Monget, J., Albuisson, M., Guillard, H., Regas, N., & Wald, L.(1986). A method for the determination of the global solar radiation from meteorological satellite data. Solar Energy, 37, 31-39

Cebecauer T., (2011) MACC aerosols in solar radiation modeling for energy applications. Presentation. MACC Conference on Monitoring and Forecasting Atmospheric Composition, May 2011, Utrecht, Netherlands.

Dagestad, K. F. and Olseth, J. A., (2007). A modified algorithm for calculating the cloud index. Solar Energy. 81, 280-289.

Derrien M., H. Gleau (2005) MSG/SEVIRI cloud mask and type from SAFNWC, International Journal of Remote Sensing, 26, 4707-4732.

Dumortier, D. (1995) Modelling global and diffuse horizontal irradiances under cloudless skies with different turbidities. Daylight II, JOU2-CT92-0144, Final Report Vol. 2.

Dumortier, D. (1998) The Satellight model of turbidity variations in Europe. Technical Report Satellight Project.

Espinar B, Ramirez L, Drews D, Beyer H.G, Zarzalejo L.F, Polo J, Martin L. (2009) Analysis of different comparison parameters applied to solar radiation data from satellite and German radiometric stations, *Solar Energy* 83 (2009) 118–125

Fontoynont, M. et al. (1998) Satellight: A WWW server which provides high quality daylight and solar radiation data for Western and Central Europe. Proc. 9th Conference on Satellite Me- teorology and Oceanography, Paris, 25-29 May, 1998, 434–437.

Gueymard C. (1989) A two-band model for the calculation of clear sky solar irradiance, illuminance, and photosynthetically active radiation at the earth surface. Solar Energy, Vol. 43, N° 5, 253-265.

Hammer, A., D. Heinemann and A. Westerhellweg (1998) Derivation of daylight and solar irradiance data from satellite observations. Proc. 9th Conference on Satellite Meteorology and Oceanography, Paris, 25-29 May, 1998, 747–750.

Hammer, A., (2000) Anwendungsspezifische Solarstrahlungsinformation aus METEOSAT-Daten, Dissertation, Universität Oldenburg, http://oops.uni-oldenburg.de/317/

Hammer A, Heinemann D, Hoyer C, Kuhlemann R, Lorenz E, Müller R, Beyer HG (2003): Solar energy assessment using remote sensing technologies. Remote Sensing of Environment, 86, 423–432.

Hammer A, Lorenz E, Kemper A, Heinemann D, Beyer HG, Schumann K, Schwandt M (2009): 'Direct normal irradiance for CSP based on satellite images of Meteosat Second Generation', SolarPACES 2009, Berlin

Ineichen P. (2008) A broadband simplified version of the Solis clear sky model, Solar Energy 82, 758–762.

Ineichen P. (2008c). Comparison and validation of three global-to-beam irradiance models against ground measurements. Sol. Energy , doi:10.1016/ j.solener.2007.12.006

Ineichen P., Barroso C., Geiger B., Hollmann R., Marsouin A., Mueller R. (2009) Satellite Application Facilities irradiance products: hourly time step comparison and validation over Europe. International Journal of Remote Sensing, Vol. 30, No. 21, 5549–5571.

Ineichen P. (2010) Aerosol quantification based on global irradiance. Solar Paces 2010, Perpignan France

Ineichen P. (2011) Five satellite products deriving beam and global irradiance validation on data from 23 ground stations, University of Geneva
http://archive-ouverte.unige.ch/unige:23669

Kalnay E et al. (1996): The NMC/NCAR 40-year reanalysis project. Bull. Am. Meteorol. Soc. 77 (3), 437–472.

Kasten F. (1980) A simple parameterization of two pyrheliometric formulae for determining the Linke turbidity factor. Meteor. Rdsch. 33, 124–127.

Kinne, S. et al (2005) An AeroCom initial assessment optical properties in aerosol component modules of global models Atmos. Chem. Phys. Discuss., **5**, 1-46.

Kinne, S. (2008), Clouds in the perturbed climate system, chap. Climatologies of cloud related aerosols: Particle number and size, ISBN: 978-0-262-01287-4, The MIT Press.

Liu B.Y.H, Jordan R.C (1960) The interrelationship and characteristic distribution of direct, diffuse and total solar radiation. Volume 4, Issue 3, Pages 1-19

Lorenz E. (2007): Improved diffuse radiation model, MSG. Report for the EC-project PVSAT-2: Intelligent Performance Check of PV System Operation

Louche, A., Notton, G., Poggi, P. and Simonnot, G., (1991). Correlations for direct normal and global horizontal irradiation on a French Mediterranean site. Solar Energy. 46, 261-266.

Massey Jr., F.J., (1951) The Kolmogorov–Smirnov test for goodness of fit. Journal of the American Statistical Association 4, 68–78.

Meyer, Richard und Lohmann, Sina und Schillings, Christoph und Hoyer, Carsten, (2006) Climate Statistics for Planning and Siting of Solar Energy Systems: Long-Term Variability of Solar Radiation Derived from Satellite Data. In: Nova Science Publishers Earthlink, pages 55-68. ISBN 1-59454-919-2

Mayer, B., and A. Kylling (2005), Technical note: The libradtran software package for radiative transfer calculations - description and examples of use, Atmospheric Chemistry and Physics, 5, 1855–1877.

Molineaux B., Ineichen P., O'Neill N.T (1998). Equivalence of pyrheliometric and aerosol optical depth at a single wavelength. Appl. Opt., 37, 7008-7018.

Möser, W., and E. Raschke (1984), Incident solar-radiation over europe estimated from meteosat data, J Clim Appl Meteorol, 23(1), 166–170.

Müller, R., et al. (2004), Rethinking satellite-based solar irradiance modelling – the solis clear-sky module, Remote Sensing of Environment, 91(2), 160–174, doi:10.1016/j.rse.2004.02.009.

Müller, R. W., C. Matsoukas, A. Gratzki, H. D. Behr, and R. Hollmann (2009), The cm-saf operational scheme for the satellite based retrieval of solar surface irradiance - a lut based eigenvector hybrid approach, Remote Sensing of Environment, 113(5), 1012–1024, doi:10.1016/j.rse.2009.01.012.

Page, J. (1996) Algorithms for the Satellight programme. Technical report.

Perez R., R. Seals, P. Ineichen, R. Stewart, D. Menicucci (1987) A New Simplified Version of the Perez Diffuse Irradiance Model for Tilted Surfaces. Description Performance Validation. Solar Energy, 39, 221-232.

Perez R., Ineichen P., Seals R., Zelenka A. (1990) Making full use of the clearness index for parametrizing hourly insolation conditions. Solar Energy 45, N° 2, 111-114.

Perez R., P. Ineichen, E. Maxwell, R. Seals, A. Zelenka (1992) Dynamic global to direct irradiance conversion models. ASHARE Trans. Res. Series, 1992, 354-369

Polo, J., Zarzalejo, L. F., Martin, L., Navarro, A. A. and Marchante, R., (2009a) Estimation of daily Linke turbidity factor by using global irradiance measurements at solar noon. Solar Energy. 83, 1177-1185.

Polo, J., Zarzalejo, L. F., Salvador, P. and Ramírez, L. (2009b) Angstrom turbidity and ozone column estimations from spectral solar irradiance in a semi-desertic environment in Spain. Solar Energy. 83, 257-263.

Remund J. (2009): Aerosol optical depth and Linke turbidity climatology, Description for final report of IEA SHC Task 36, Meteotest Bern

Rigollier C., Bauer O., Wald L. (2000) On the Clear Sky Model of the ESRA - european Solar Radiation Atlas - with Respect to the Heliosat Method. Solar Energy **68** (1), 33-48.

Rigollier C., Lefèvre M, Wald L. (2004) The method heliosat-2 for deriving shortwave solar irradiance radiation from satellite imagesSolar Energy, 77(2), 159-169

Ruiz-Arias J.A., T. Cebecauer, J. Tovar-Pescador, M. Šúri, (2010). Spatial disaggregation of satellite-derived irradiance using a high resolution digital elevation model, accepted to Solar Energy.

Ruyter de Wildt M., G. Seiz, A. Gruen (2007) Operational snow mapping using multitemporal Meteosat SEVIRI imagery, Remote Sensing of Environment, 109, 29-41.

Skartveit, A. and J. A. Olseth (1987) A Model for the Diffuse Fraction of Hourly Global Radiation. Solar Energy 38, 271–274.

Skartveit, A., J. A. Olseth and M. E. Tuft (1998) An hourly diffuse fraction model with correction for variability and surface albedo. Solar Energy 63, 173–183.

Stoekli R. (2013) The HelioMont Surface Solar Radiation Processing. Scientific Report MeteoSwiss No. 93

Vernez D., Bulliard J.L., Vuilleumier L., Moccozet L., Milon A. (2013) The effects of UV radiation in terrain on human health. FOKO 3012-1, MeteoSwiss, Zurich.

Zarzalejo L.F., Jesús Polo, Luis Martín, Lourdes Ramírez, Bella Espinar (2009) A new statistical approach for deriving global solar radiation from satellite images. Solar Energy, Volume 83, Issue 4, Pages 480-484

Zelenka, A., R. Perez, R. Seals and D. Renné (1998) Effective accuracy of models converting atellite radiances to hourly surface insolation. Proc. 9th Conference on Satellite Meteorology and Oceanography, Paris, 25-29 May, 1998, 710–713.

Zelenka, A. (2004) ENVISOLAR Project - Environmental Information for Solar Energy Industries, project report no. 6 'Science Review'

Long term satellite hourly, daily and monthly global, beam and diffuse irradiance validation. Interannual variability analysis.

Annex

The following pages for the site of Almeria and the SolarGis model describe the figures given in the different annexes for each site.

The annexes can be downloaded from:

http://www.unige.ch/energie/forel/energie/equipe/ineichen/annexes-iae.html

or from

http://www.cuepe.ch/archives/annexes-iae/annex-saf-vol-I.pdf
http://www.cuepe.ch/archives/annexes-iae/annex-saf-vol-II.pdf
http://www.cuepe.ch/archives/annexes-iae/annex-saf-vol-III.pdf

http://www.cuepe.ch/archives/annexes-iae/annex-almeria.pdf
http://www.cuepe.ch/archives/annexes-iae/annex-bratislava.pdf
http://www.cuepe.ch/archives/annexes-iae/annex-carpentras.pdf
http://www.cuepe.ch/archives/annexes-iae/annex-davos.pdf
http://www.cuepe.ch/archives/annexes-iae/annex-kassel.pdf
http://www.cuepe.ch/archives/annexes-iae/annex-lerwick.pdf
http://www.cuepe.ch/archives/annexes-iae/annex-lindenberg.pdf
http://www.cuepe.ch/archives/annexes-iae/annex-madrid.pdf
http://www.cuepe.ch/archives/annexes-iae/annex-nantes.pdf
http://www.cuepe.ch/archives/annexes-iae/annex-sedeboqer.pdf
http://www.cuepe.ch/archives/annexes-iae/annex-tamanrasset.pdf
http://www.cuepe.ch/archives/annexes-iae/annex-toravere.pdf
http://www.cuepe.ch/archives/annexes-iae/annex-valentia.pdf
http://www.cuepe.ch/archives/annexes-iae/annex-vaulx.pdf
http://www.cuepe.ch/archives/annexes-iae/annex-wien.pdf
http://www.cuepe.ch/archives/annexes-iae/annex-zilani.pdf

Figures

Tables

Table a-I*n* Site by site and model by model hourly global/beam/diffuse irradiance validation results expressed in relative and absolute values. The absolute values are given in [Wh/m2h].
For all sites, the overall values, the absolute mean bias and the standard deviation of the bias are given.

Table a-II*n* Site by site and model by model daily global/beam/diffuse irradiance validation results expressed in relative and absolute values. The absolute values are given in [kWh/m2day].
For all sites, the overall values, the absolute mean bias and the standard deviation of the bias are given.

Table a-III*n* Site by site and model by model monthly global/beam/diffuse irradiance validation results expressed in relative and absolute values. The absolute values are given in [kWh/m2month].
For all sites, the overall values, the absolute mean bias and the standard deviation of the bias are given.

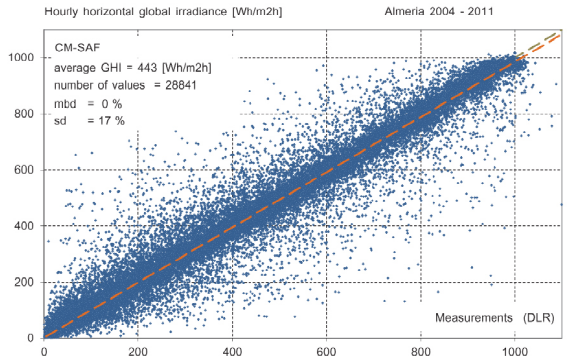

Figure a-1g Model versus measurements for hourly global irradiance

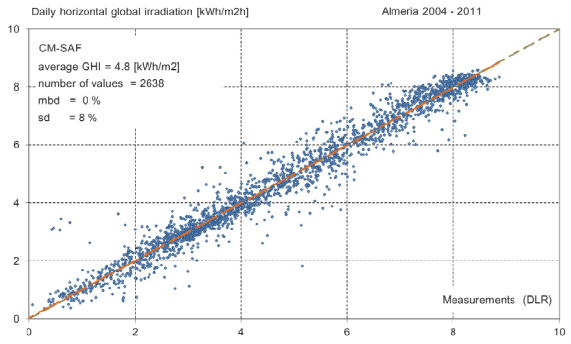

Figure a-2g Model versus measurements for daily global irradiance
Units: [kWh/m^{2}day]

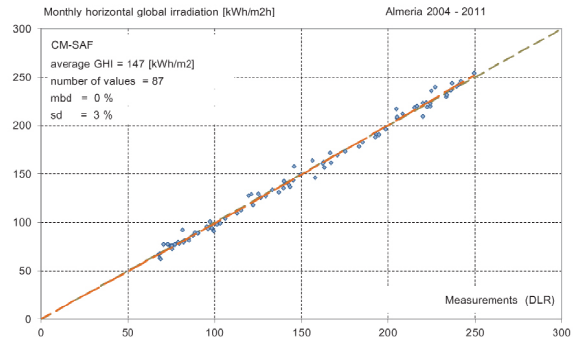

Figure a-3g Model versus measurements for monthly global irradiance
Units: [kWh/m^{2}month]

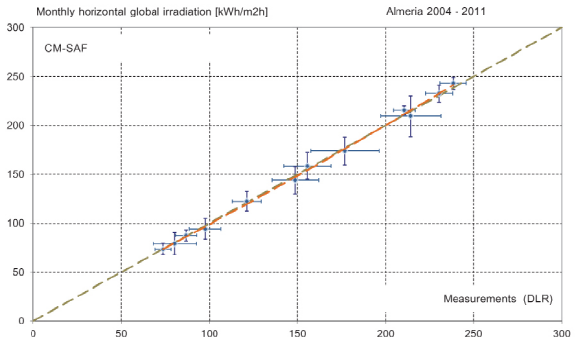

Figure a-4g Model versus measurements for monthly average global irradiance, surrounded by ± one standard deviation on each axis
Units: [kWh/m^{2}month]

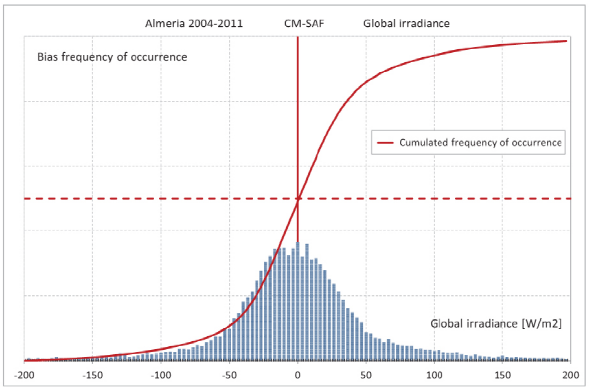

Figure a-5g Hourly values distribution of the model-measurements difference around the 1:1 axis of Fig 14 for the all the data. The corresponding cumulated curve is also represented

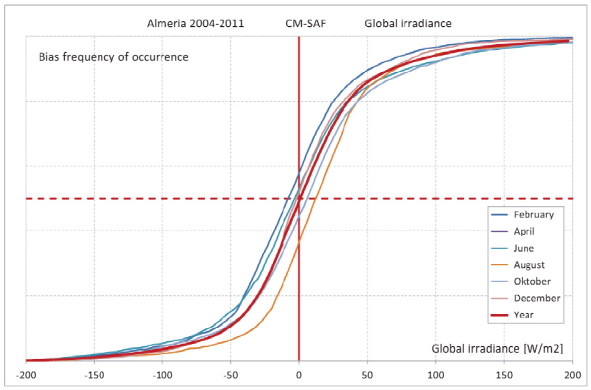

Figure a-6g Cumulated frequency of occurrence of the model-measurements difference versus the model-measurements difference

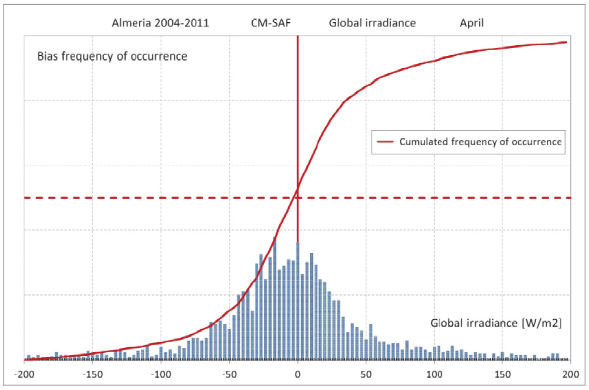

Figure a-7g same as Fig 18 for April

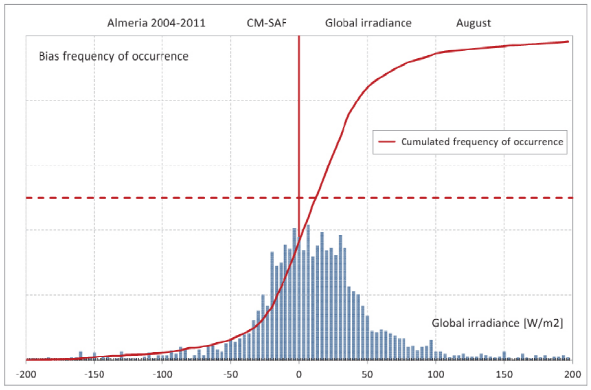

Figure a-8g same as Fig 18 for August

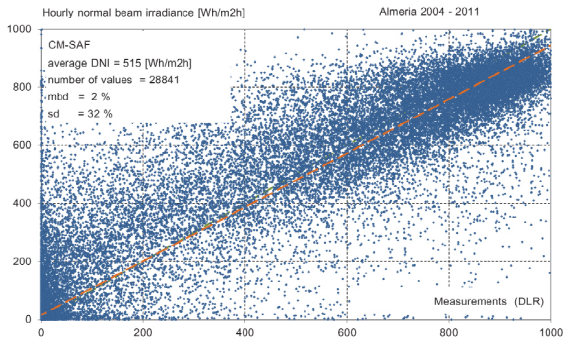

Figure a-1b Model versus measurements for hourly beam irradiance

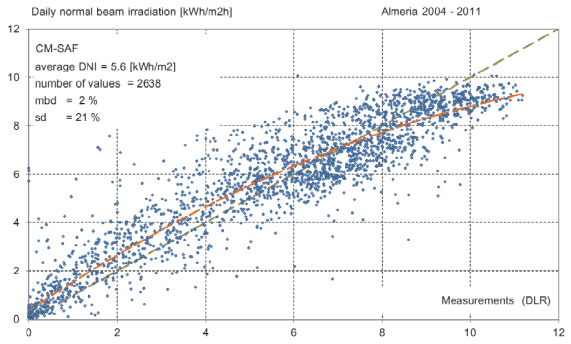

Figure a-2b Model versus measurements for daily beam irradiance
Units: [kWh/m²day]

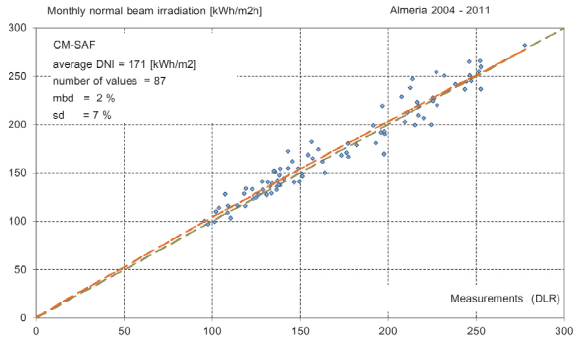

Figure a-3b Model versus measurements for monthly beam irradiance
Units: [kWh/m²month]

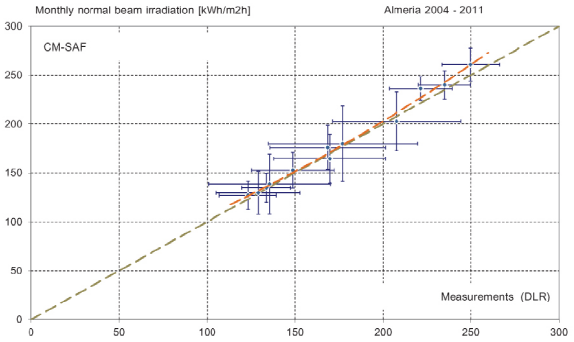

Figure a-4b Model versus measurements for monthly average beam irradiance, surrounded by ± one standard deviation on each axis
Units: [kWh/m²month]

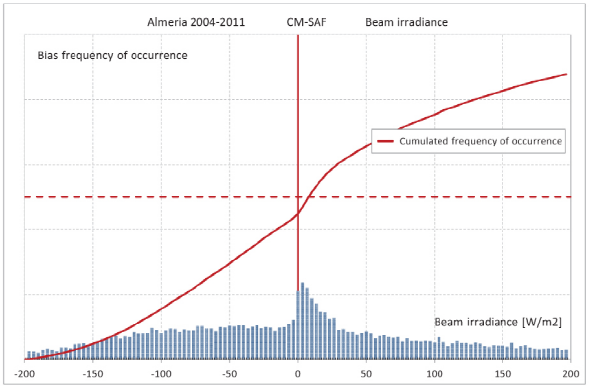

Figure a-5b Hourly values distribution of the model-measurements difference around the 1:1 axis of Fig 14 for the all the data. The corresponding cumulated curve is also represented

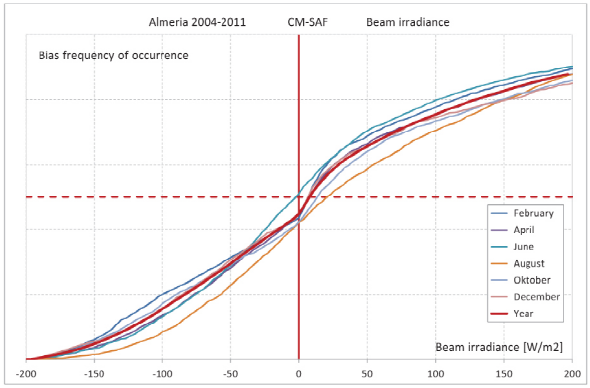

Figure a-6b Cumulated frequency of occurrence of the model-measurements difference versus the model-measurements difference

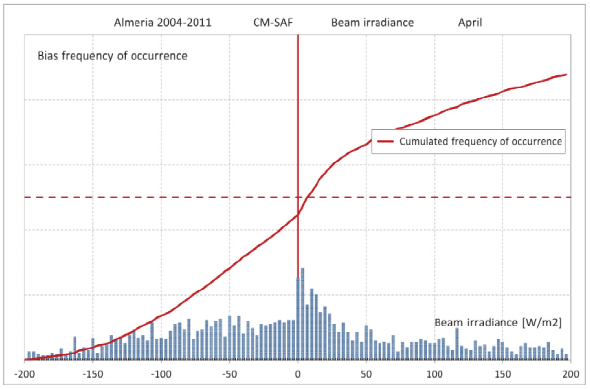

Figure a-7b same as Fig 18 for April

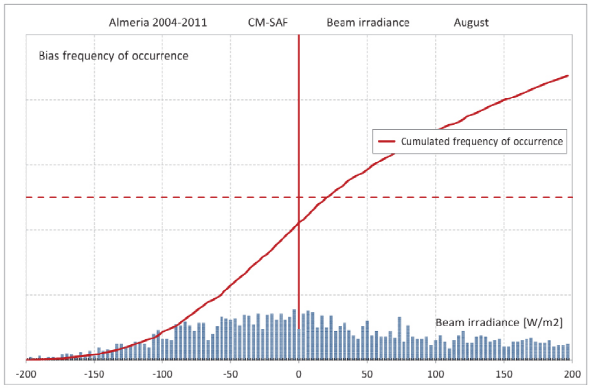

Figure a-8b same as Fig 18 for August

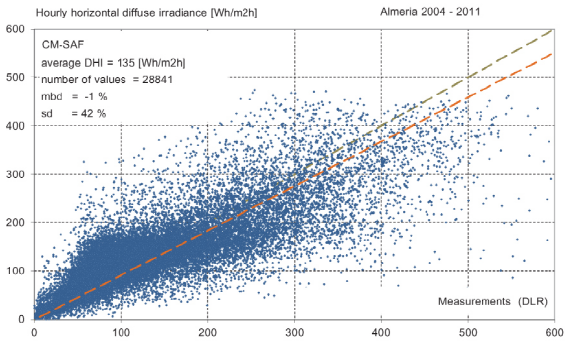

Figure a-1d Model versus measurements for hourly diffuse irradiance

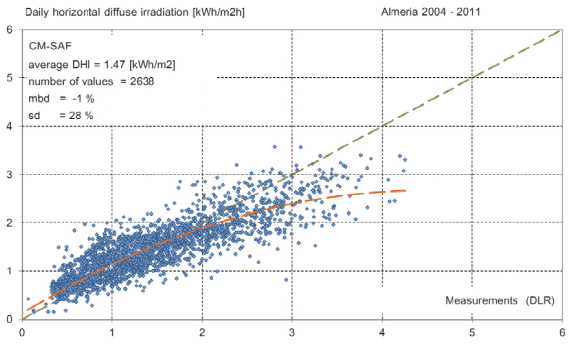

Figure a-2d Model versus measurements for daily diffuse irradiance
Units: [kWh/m^{2}day]

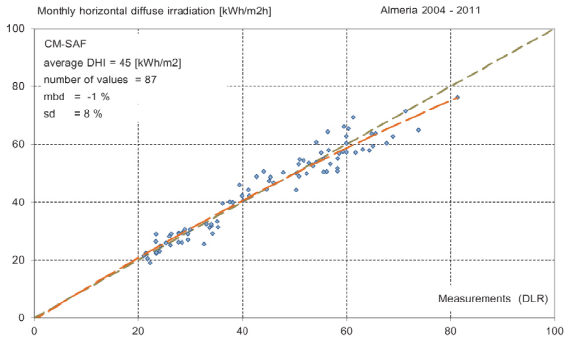

Figure a-3d Model versus measurements for monthly diffuse irradiance
Units: [kWh/m^{2}month]

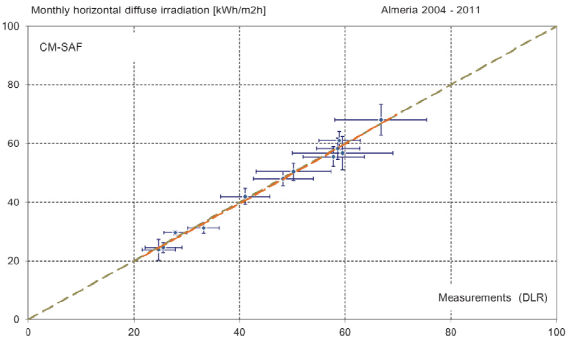

Figure a-4d Model versus measurements for monthly average diffuse irradiance, surrounded by ± one standard deviation on each axis
Units: [kWh/m^{2}month]

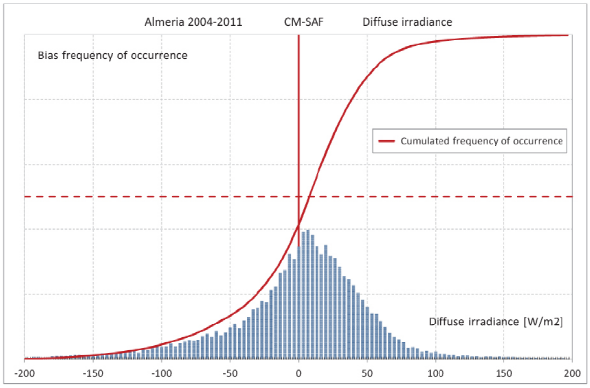

Figure a-5d Hourly values distribution of the model-measurements difference around the 1:1 axis of Fig 14 for the all the data. The corresponding cumulated curve is also represented

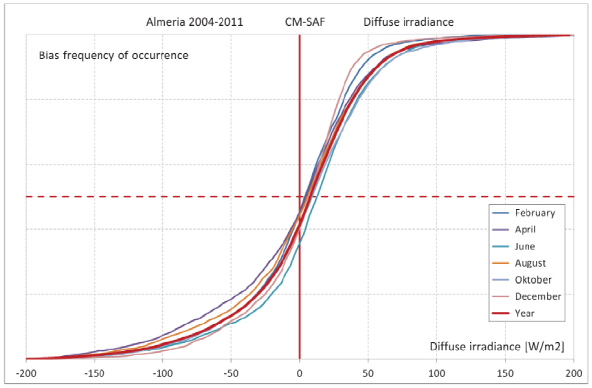

Figure a-6d Cumulated frequency of occurrence of the model-measurements difference versus the model-measurements difference

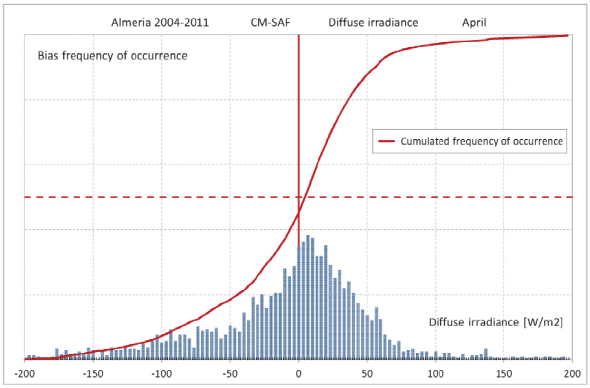

Figure a-7d same as Fig 18 for April

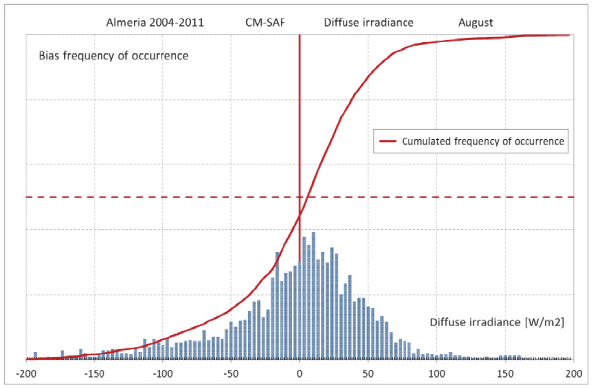

Figure a-8d same as Fig 18 for August

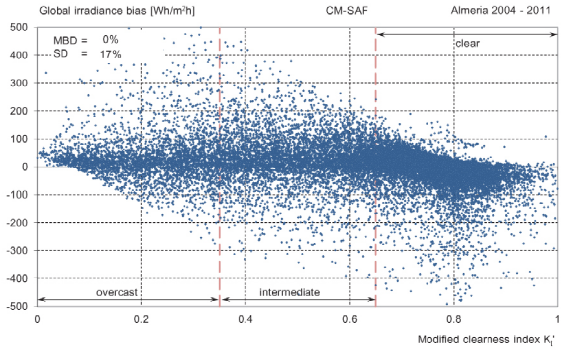

Figure a-9g Model-measurements difference for hourly global irradiance values versus the modified clearness index K_t'

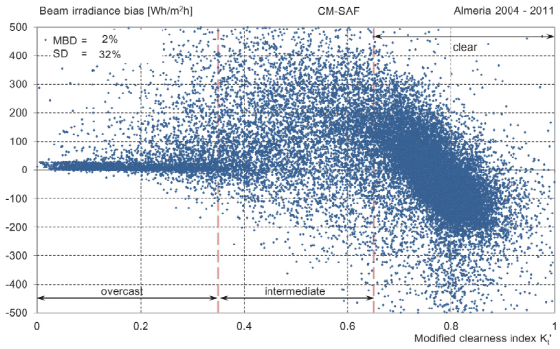

Figure a-9b Model-measurements difference for hourly normal beam irradiance values versus the modified clearness index K_t'

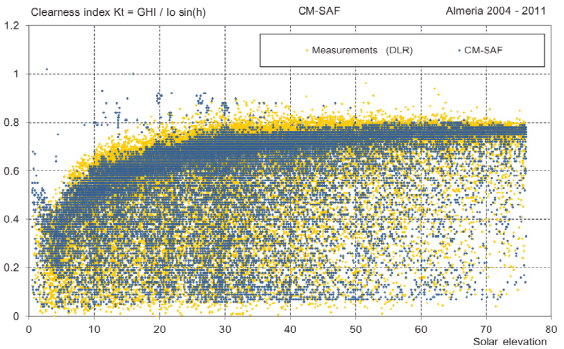

Figure a-10g Clearness index K_t versus the solar elevation angle for the measurements (yellow) and the modeled (blue) hourly values

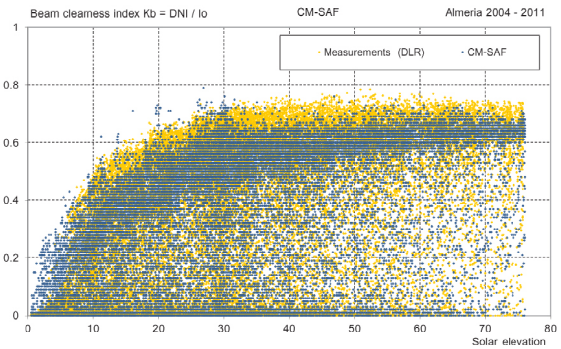

Figure a-10b Beam clearness index K_b versus the solar elevation angle for the measurements (yellow) and the modeled (blue) hourly values

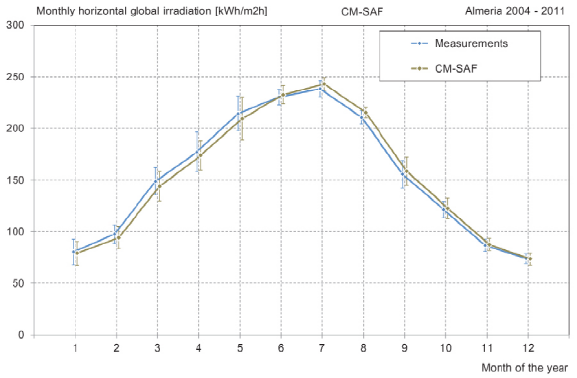

Figure a-11g Monthly averaged values surrounded by ± one standard deviation for the modeled and the measured values of the global irradiance.
Units: [kWh/m²month]

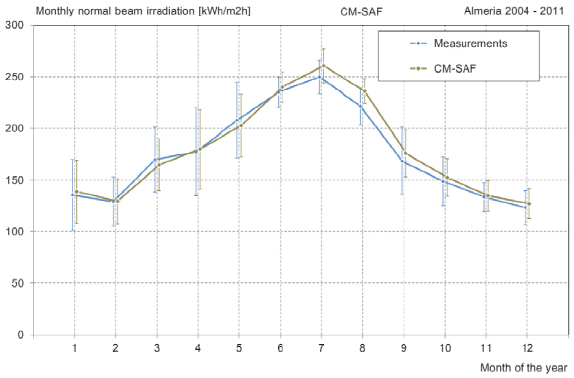

Figure a-11b Monthly averaged values surrounded by ± one standard deviation for the modeled and the measured values of the normal beam irradiance.
Units: [kWh/m²month]

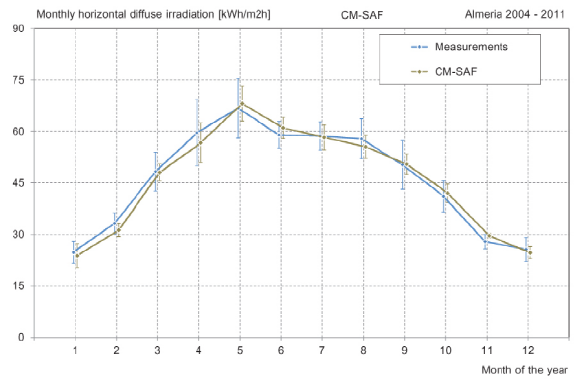

Figure a-11d same as Fig a-11g for the diffuse irradiance. Units: [kWh/m²month]

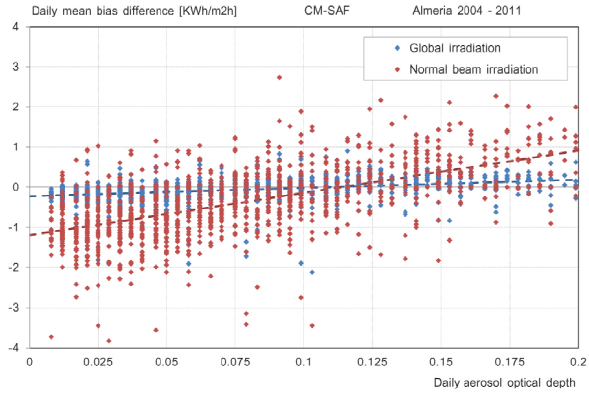

Figure aod Model bias versus the aod evaluated from ground beam irradiance measurements

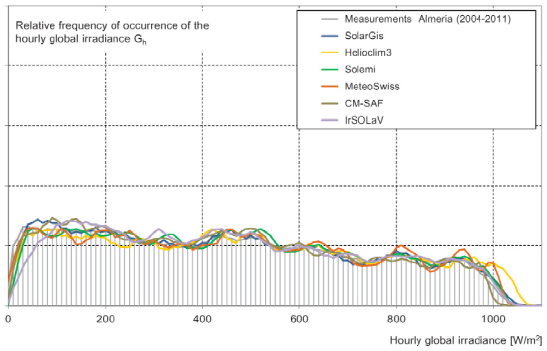

Figure a-12g Relative frequency of occurrence of the hourly global irradiance versus the corresponding irradiance. The measurements are represented in grey.

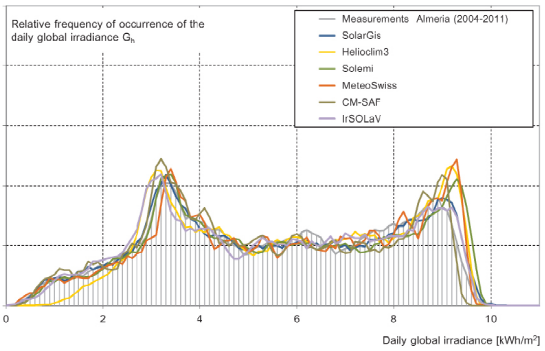

Figure a-13g Relative frequency of occurrence of the daily global irradiance versus the corresponding irradiance. The measurements are represented in grey.

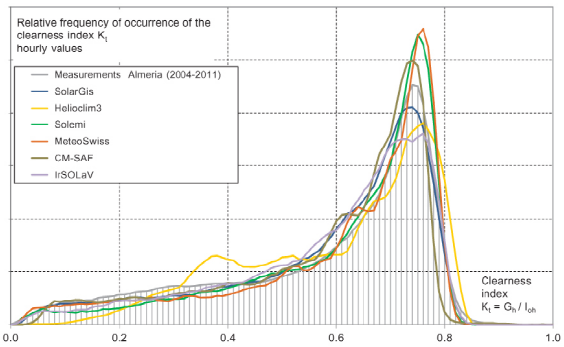

Figure a-14g Relative frequency of occurrence of the global clearness index versus the corresponding clearness index K_t. The measurements are represented in grey.

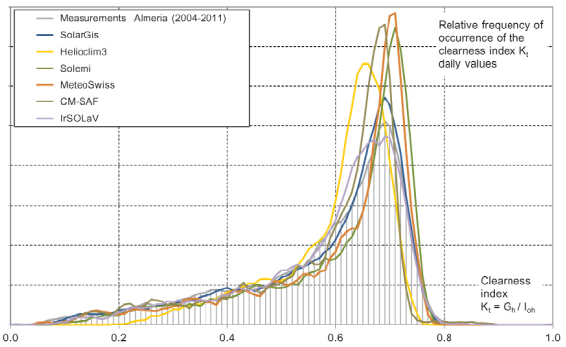

Figure a-15g Relative frequency of occurrence of the daily global clearness index versus the corresponding clearness index. The measurements are represented in grey.

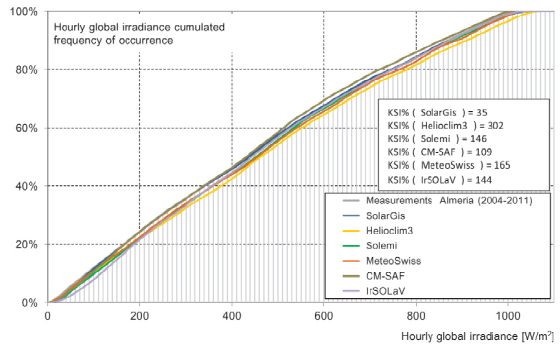

Figure a-16g Cumulated frequency of occurrence of the hourly global irradiance values versus the corresponding irradiance. The measurements are represented in grey.

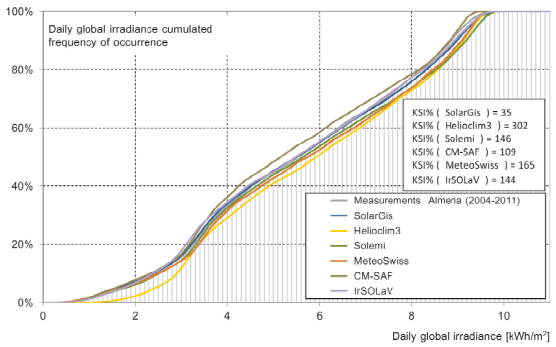

Figure a-17g Cumulated frequency of occurrence of the daily global irradiance values versus the corresponding irradiance. The measurements are represented in grey.

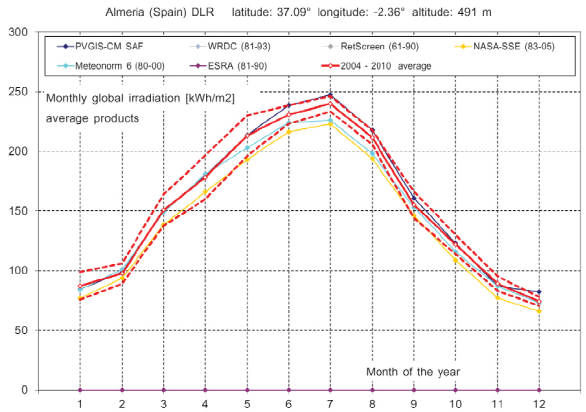

Figure a-18g Monthly averaged values of the global irradiation for the average models. Dashed line represent ± one *sd* around the measurements

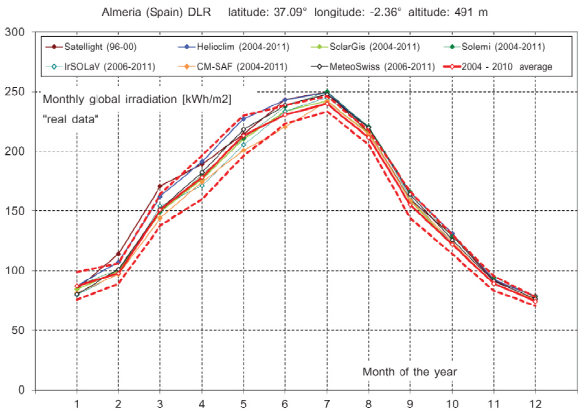

Figure a-19g Monthly averaged values of the global irradiation for the «real time» models. Dashed line represent ± one *sd*

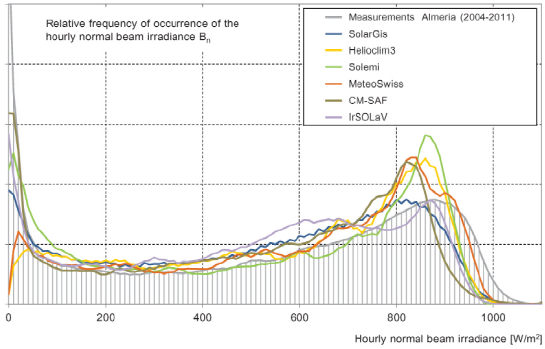

Figure a-12b Relative frequency of occurrence of the hourly beam irradiance versus the corresponding irradiance. The measurements are represented in grey.

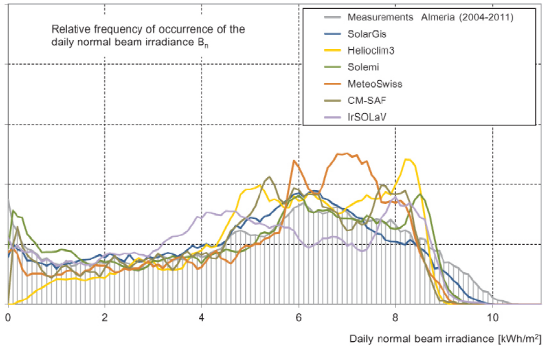

Figure a-13b Relative frequency of occurrence of the daily beam irradiance versus the corresponding irradiance. The measurements are represented in grey.

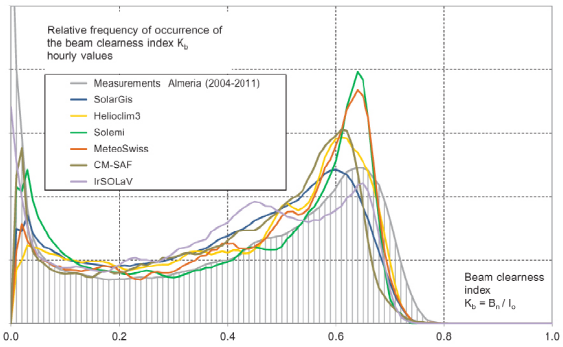

Figure a-14b Relative frequency of occurrence of the beam clearness index versus the corresponding clearness index K_t. The measurements are represented in grey.

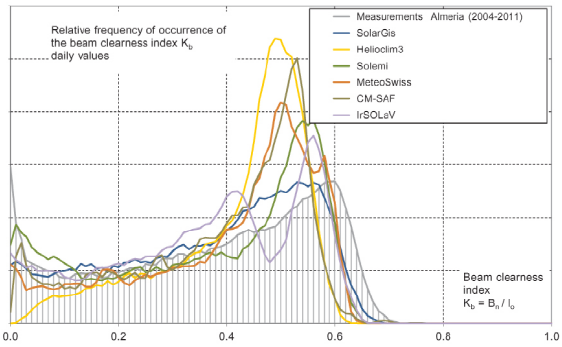

Figure a-15b Relative frequency of occurrence of the daily beam clearness index versus the corresponding clearness index. The measurements are represented in grey.

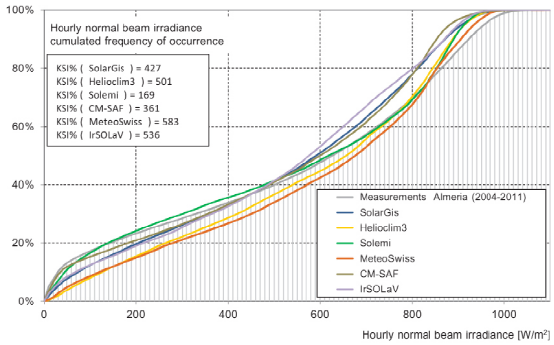

Figure a-16b Cumulated frequency of occurrence of the hourly beam irradiance values versus the corresponding irradiance. The measurements are represented in grey.

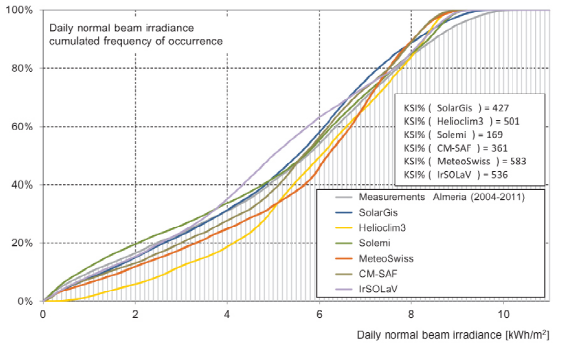

Figure a-17b Cumulated frequency of occurrence of the daily beam irradiance values versus the corresponding irradiance. The measurements are represented in grey.

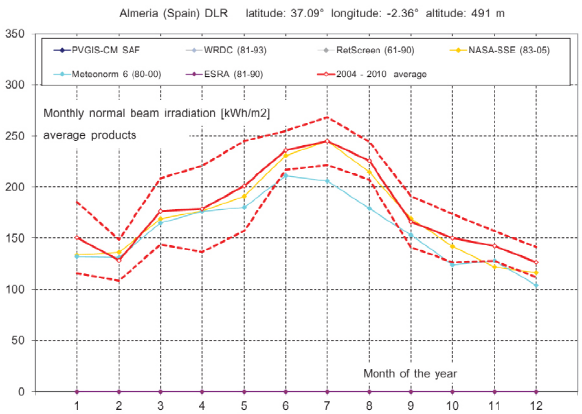

Figure a-18b Monthly averaged values of the beam irradiation for the average models. Dashed line represent ± one *sd* around the measurements

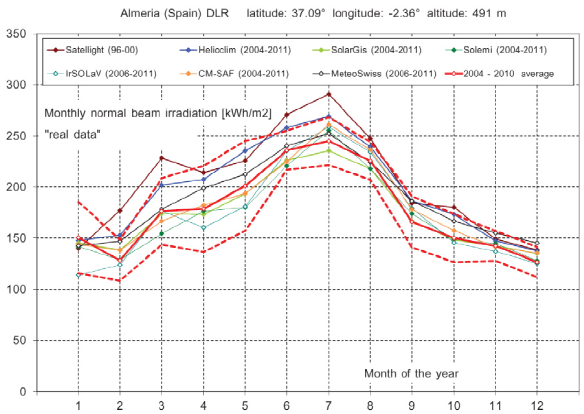

Figure a-19b Monthly averaged values of the beam irradiation for the «real time» models. Dashed line represent ± one *sd*

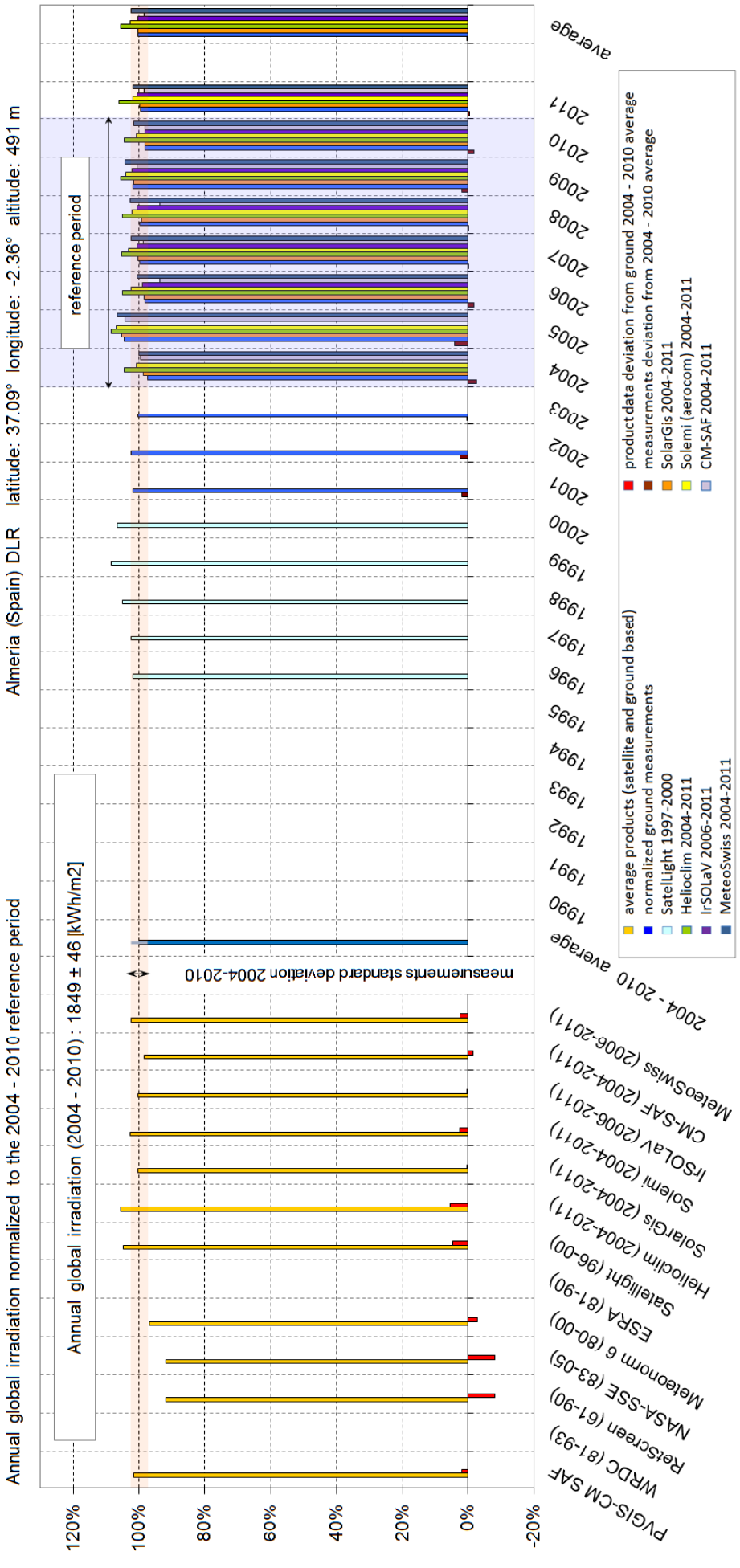

Figure a-20g Interannual variability of the global irradiation for the measurements, the average models, and the nowcasting products. The values are normalized to the 2004-2010 reference period average.

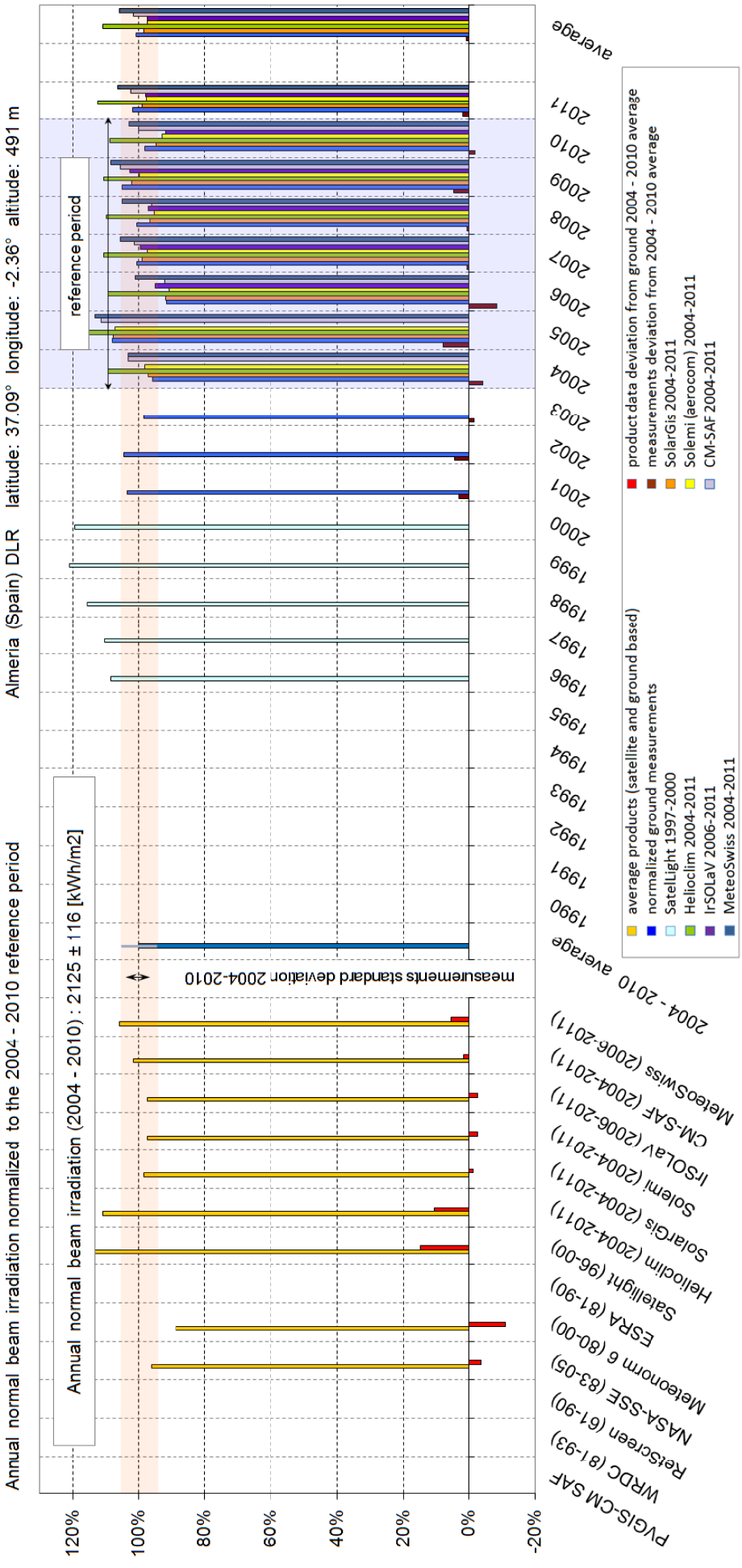

Figure a-20b Interannual variability of the normal beam irradiation for the measurements, the average models, and the nowcasting products. The values are normalized to the 2004-2010 reference period average.